DAHLGREN DIVISION
NAVAL SURFACE WARFARE CENTER
Dahlgren, Virginia 22448-5100

NSWCDD/TR-97/3

ELECTROMAGNETIC REMOTE SENSING FOR AIRFIELD ASSESSMENT

BY NANCY SWANSON VICTORIA IRWIN DAVID MARCHETTE

SYSTEMS RESEARCH AND TECHNOLOGY DEPARTMENT

JANUARY 1997

REPORT DOCUMENTATION PAGE

Form Approved
OMB No. 0704-0188

1. AGENCY USE ONLY (Leave blank)	2. REPORT DATE	3. REPORT TYPE AND DATES COVERED
	January 1997	Final

4. TITLE AND SUBTITLE

Electromagnetic Remote Sensing for Airfield Assessment

5. FUNDING NUMBERS

6. AUTHOR(s)

Nancy Swanson, Victoria Irwin, David Marchette

7. PERFORMING ORGANIZATION NAME(S) AND ADDRESS(ES)

Commander
Naval Surface Warfare Center
Dahlgren Division (Code B10)
17320 Dahlgren Road
Dahlgren, VA 22448-5100

8. PERFORMING ORGANIZATION REPORT NUMBER

NSWCDD/TR-97/3

9. SPONSORING/MONITORING AGENCY NAME(S) AND ADDRESS(ES)

WL/FIVCO-0L (Dr. J. W. Rish), Wright Laboratory
Stop 37, 139 Barnes Drive, Suite 2
Tydall Air Force Base, FL 32403

10. SPONSORING/MONITORING AGENCY REPORT NUMBER

11. SUPPLEMENTARY NOTES

12a. DISTRIBUTION/AVAILABILITY STATEMENT

Approved for public release; distribution is unlimited.

12b. DISTRIBUTION CODE

13. ABSTRACT (Maximum 200 words)

The subject of this report is a study of current state-of-the-art electro-optical systems used in remote sensing. Various passive and active imaging systems were analyzed for application to remote sensing of airfields. Descriptions of systems are included. The purpose was to determine an effective standoff sensing of the safety of remote airfields, especially when hostilities are underway. Criteria of interest were type of material (including differences in material, such as patches), delamination, cracks, holes, spalls, debris, surface roughness (large scale, such as trenches) and subsurface voids. Detailed results are included, supplemented with illustrations, as well as a summary of findings. The conclusion was that a combination of imaging systems is necessary to detect all of the defects. Recommendations include that the thermal imaging system, which yielded the most information, be further studied for this purpose. Enhancements to the thermal system were also recommended. Further study was recommended to determine if the thermal system can distinguish runway material (asphalt, concrete, etc.) based on knowledge of material properties (emissivity, thermal conductivity, and heat capacity) and ambient temperature.

14. SUBJECT TERMS

electro-optical systems, blackbody, thermal, staring system, scanning system, infrared, charge coupled device (CCD), multispectral imaging, hyperspectral, stereoscopic, polarimetry, Light Detection and Ranging (LIDAR)

15. NUMBER OF PAGES

76

16. PRICE CODE

17. SECURITY CLASSIFICATION OF REPORTS	18. SECURITY CLASSIFICATION OF THIS PAGE	19. SECURITY CLASSIFICATION OF ABSTRACT	20. LIMITATION OF ABSTRACT
UNCLASSIFIED	UNCLASSIFIED	UNCLASSIFIED	UL

FOREWORD

The subject of this report is a study of current state-of-the-art electro-optical systems used in remote sensing. The purpose was to determine an effective standoff sensing of the safety of remote airfields, especially when hostilities are underway. Data produced by these systems would complement combat control team findings currently in use and provide a nondestructive pavement analysis system to augment peacetime evaluation techniques.

The author would like to thank the project's sponsor, Dr. Jeff Rish of Wright Laboratory, Tyndall Air Force Base (TAFB), Florida. The author is also indebted to the following people for their valuable contributions to this project: Hugh Welker of Applied Research Associates, TAFB, and Brad Blume of Nichols Research Corporation, Panama City Beach, Florida. Hugh Welker prepared the test runway at TAFB for the field test. He also assisted in taking data during the field test. Brad Blume assisted in taking data during the field test and in analyzing some of the thermal data.

This document has been reviewed by Stuart L. Moran, Head, Pulsed Power Systems and Technology Group.

Approved by:

MARY E. LACEY, Head
Systems Research and Technology Department

CONTENTS

ILLUSTRATIONS

ILLUSTRATIONS (Continued)

ILLUSTRATIONS (Continued)

TABLES

CHAPTER 1

INTRODUCTION

U.S. Air Force responsibilities require that field units can perform quick, accurate assessments of pavement conditions at remote operating locations. A standoff assessment is necessary when these "quick-look" evaluations must be accomplished in areas where hostilities are known to be underway. The evaluation system should provide enough information to independently assess the pavement conditions in times of dire need. In less stringent environments, data produced by these systems would complement the findings of the combat control teams currently in use. It would also provide a non-destructive pavement analysis system to augment peacetime pavement evaluation techniques.

The study is confined to the evaluation of electro-optical systems for this application. Both active (laser source) and passive (ambient source) systems have been assessed. The sensors that have been evaluated are limited to the visible (0.40-0.75 μm), the near infrared (IR) (0.75-1.0 μm), the mid IR (1.0-6.0 μm), and the far IR (6.0-12.0 μm). The mid and far IR are in the region of blackbody or thermal radiation. There does not exist a single detector for this entire range of electro-magnetic energy. If information from more than one range is required, then it will be necessary to incorporate multiple detectors in the system.

In Chapter 2, the various types of detectors are discussed. The concepts of resolution, frame rates, field-of-view (FOV), and scan rates for remote sensing systems are introduced. Chapter 3 contains a detailed description of the passive imaging systems as applied to standoff pavement evaluation. The active imaging systems are discussed in Chapter 4. In Chapter 5 the results of the field test performed at Wright Laboratory in September of 1996 are reported. Results of the image processing on the data collected in Chapter 5 are covered in Chapter 6. Chapters 7 and 8 are the summary and recommendations resulting from this study.

CHAPTER 2

BACKGROUND

Many advanced optical systems have been developed for remote sensing. The sensors can be classified into two types: staring systems or scanning systems. The detectors employed in the staring systems are most commonly Charge Coupled Device (CCD) cameras. The CCD consists of a fixed, two dimensional photodiode (pixel) array for any given camera. The CCD camera is employed in both active and passive remote sensing. The scanning systems are either a line scan system or a beam fanning system. The line scan system has been applied to both active and passive imaging systems. It consists of a single detector, such as a photomultiplier tube, which scans in the x-direction while the motion of the platform yields the y-direction. In this way a two dimensional image is reconstructed. A beam fanning system consists of producing a fan beam from a laser beam by expanding the beam in the x-direction, but not the y-direction. The detector is a one dimensional photodiode array that detects the fan beam in the x-direction. The y-direction is obtained from the forward motion of the platform. The two dimensional image is reconstructed from the sequential series of data stream output from the diode array.

In all cases the obtained image is "pixelated" or digitized. The resolution of a given sensor system will depend on the pixel size, the focusing optics and the distance from the target. From Figure 2-1, clearly

$$\tan(\theta) = \frac{X_{pix}}{2f} = \frac{X_{eff}}{2L}, \tag{2-1}$$

where

$$L = \frac{h}{\cos(\varphi)}, \tag{2-2}$$

x_{pix} is the length of a single pixel, θ is the half angle subtended by a single pixel at the center of the focusing lens, h is the height of the sensor above the ground, φ is the look angle of the sensor measured from vertical, and x_{eff} is the effective length subtended by a single pixel at the surface of the pavement. Combining Equations (2-1) and (2-2), the effective length is then

$$X_{eff} = \frac{h\,X_{pix}}{f\cos(\varphi)}. \tag{2-3}$$

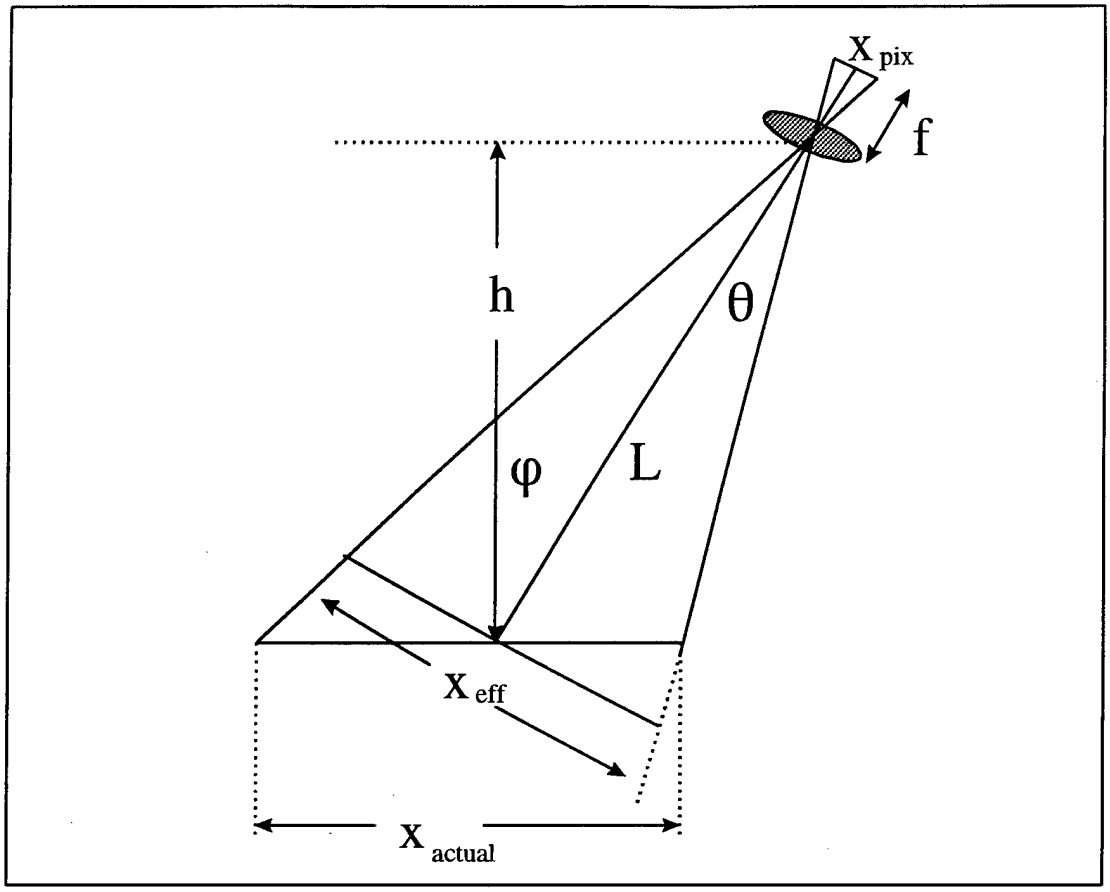

Figure 2-1. Area Subtended by a Single Pixel

We assume that $x_{eff} \cong x_{actual}$, which is valid for small look angles. For a square pixel, the effective area subtended by a single pixel at the pavement surface is

$$A_{eff} = A_{pix}\left(\frac{h}{f\cos(\varphi)}\right)^2 \tag{2-4}$$

If the look angle is zero, then Equation (2-4) reduces to

$$A_{eff} = A_{pix}\left(\frac{h}{f}\right)^2. \tag{2-5}$$

The minimum requirement for detection of a feature at the pavement surface is that dimensions of the feature are larger than the area subtended by a single pixel.

If one dimension of the feature of interest is the same size as x_{eff}, then the length of its other dimension must be greater than the length subtended by a pixel in order to detect it. A crack in the pavement, for example, would be detectable if its width was equal to x_{eff} since its length would extend over many pixels. A small hole that registers in only one pixel would not be

detectable. Typical numbers for CCD cameras are: 10 μm for the pixel size, and 16 mm for the focal length of the lens. Values for x_{eff} are shown as functions of height and look angle in Table 2-1.

Table 2-1. Length Subtended by a Single Pixel for Various Heights and Look Angles

Look Angle Height: m (ft)	0°	10°	20°
30 (98.4)	1.88 cm	1.90 cm	2.00 cm
60 (196.5)	3.75 cm	3.81 cm	3.99 cm
90 (295.3)	5.63 cm	5.71 cm	5.99 cm
120 (393.7)	7.50 cm	7.62 cm	7.98 cm

The absolute value of the magnification of the system is

$$M = \frac{f}{h}. \tag{2-6}$$

Thus, the resolution can be improved by increasing f or decreasing h, which is also obvious by inspection of Equation (2-3). However, increasing f results in decreasing the FOV of the receiver, which may not be an option. The pixel size for a line scan system is determined by the scan rate, the total distance scanned in the object plane, and the velocity of the platform. All of these parameters are adjustable and will be discussed in greater detail in Chapter 4.

The frame rates necessary to obtain data for the entire area of interest, i.e., the airfield, will be determined by FOV of the camera system and the velocity of the platform. The FOV is calculated in the same manner as the area subtended by a single pixel except that the area of the entire image at the focal plane is used instead of the area of a pixel. For a CCD camera, this would be the area of the array. For a 512X512 pixel CCD array, where each pixel has width 10 μm, the focal plane has a width of 0.51 cm. Using this value in Equation (2-3) in place of x_{pix}, the length subtended by the CCD array at the pavement surface is 9.6 m (31.5 ft) at a height of 30 m (98 ft) and zero look angle. The camera FOV for these parameters is 9.6X9.6 m^2. The frame rate must exceed the requirement that at least one frame is captured every 9.6 m. If the platform velocity is 180 kn (121.6 m/s), the minimum frame rate must be 13 frames/s in order to not miss any of the pavement area. Standard frame rates on CCD cameras are 30 or 60 frames/s but can be as much as 1000 frames/s. The FOV could be decreased by ~2 orders of magnitude (thus increasing the resolution) and imaging the length of the airfield is still possible at this platform speed. By changing the FOV, the width of the imaged area would also decrease, which may mean multiple passes over the airfield to image the entire strip. For a scan system, the scan rates are matched with the platform velocity to maintain a uniform pixel size (width equals length).

It is evident from these calculations that there are many parameters which can be modified so that an optimum system for remote airfield evaluation can be designed based on requirements.

The effect of increasing or decreasing a parameter on the FOV, resolution, scan rate, and frame rate of a system is summarized in Table 2-2. These issues are relevant to all systems evaluated in this study. The salient features of specific systems are discussed in the following two chapters.

Table 2-2. Summary of Variables Determining System Parameters for Remote Imaging

Variable	FOV	Resolution	Scan Rate	Frame Rate
Decrease pixel size	decrease	increase	increase	increase
Increase array size	increase	no effect	NA	decrease
Increase platform speed	no effect	no effect	increase	increase
Decrease platform height	increase	increase	increase	decrease
Increase viewing angle	increase	decrease	increase	decrease
Decrease focal length	increase	decrease	NA	decrease

CHAPTER 3

PASSIVE IMAGING SYSTEMS

Passive imaging systems rely on ambient background illumination from the sun. They are usually easier to implement and are generally more economical than active imaging systems. The following passive imaging systems have been studied and evaluated for application to remote airfield assessment: multispectral, hyperspectral, thermal, stereoscopic, and polarimetry.

3.1 MULTISPECTRAL

Every object has a spectral signature associated with it. When illuminated with a broadband source (such as the sun), an object will reflect specific wavelengths and absorb others. The first is its reflection spectra and the second is its absorption spectra. The reflection r, is the fraction of the total incident illumination that is reflected from the object, while the absorption a, is the fraction of the incident illumination that is absorbed. Assuming all the incident radiation is either reflected or absorbed (transmission is zero), by conservation of energy, $r + a = 1$.

Multispectral imaging consists of examining more than one spectral band (usually 6-10) of the same scene. This technique is used extensively in mine countermeasures. If the spectral signature of a certain mine is known, bandpass filters can be chosen at the peaks of its reflection spectra so that the mine stands out in the scene. Ideally, the background reflection spectra (grass, sand, etc.) will be low at the wavelengths where the reflection of the mine is high.

In most cases, the spectral signature of the object of interest is not known in advance. The filters are chosen at wavelengths where the background reflection spectra are low and non-natural objects are high. The coastal battlefield reconnaissance analysis (COBRA)[1] system uses six narrow bandpass filters, three in the visible and three in the near IR. These are mounted on a filter wheel and the wheel is attached to an intensified CCD camera. The rotation of the filter wheel is synchronized with the frame rate of the camera so that each image is taken with a different filter for six frames. Then the camera is focused on a new scene and six more images are acquired. The benefits are twofold: if the reflectivity of the mine (or other object of interest) is much greater than the background, there is a large increase in the signal-to-noise ratio (SNR); also the flashing of the images, in which the object stands out in some but not in others, catches the attention of a human observer much more so than a single image does.

Except for distinguishing between material types (e.g., dirt versus concrete) this technique is not amenable to the application of remote assessment of airstrips. Firstly, because in detecting cracks, holes, spalls, etc., we would be trying to distinguish asphalt from asphalt (or concrete

from concrete). That is, a hole in asphalt will have the same spectral signature as the bulk asphalt, therefore it would be indistinguishable. Secondly, assuming we could distinguish the hole from the asphalt, the reflectance spectra of both asphalt and concrete are relatively flat in the visible (400-700 nm) and the near IR (0.7-1.0 μm). These spectra are reproduced in Figures 3-1 and 3-2 (courtesy of J. Salisbury, Johns Hopkins University (JHU) spectral library) for weathered asphalt and concrete with limestone and quartz aggregate. Since there are no peaks or special features in these spectra (at these wavelengths), there is nothing to exploit.

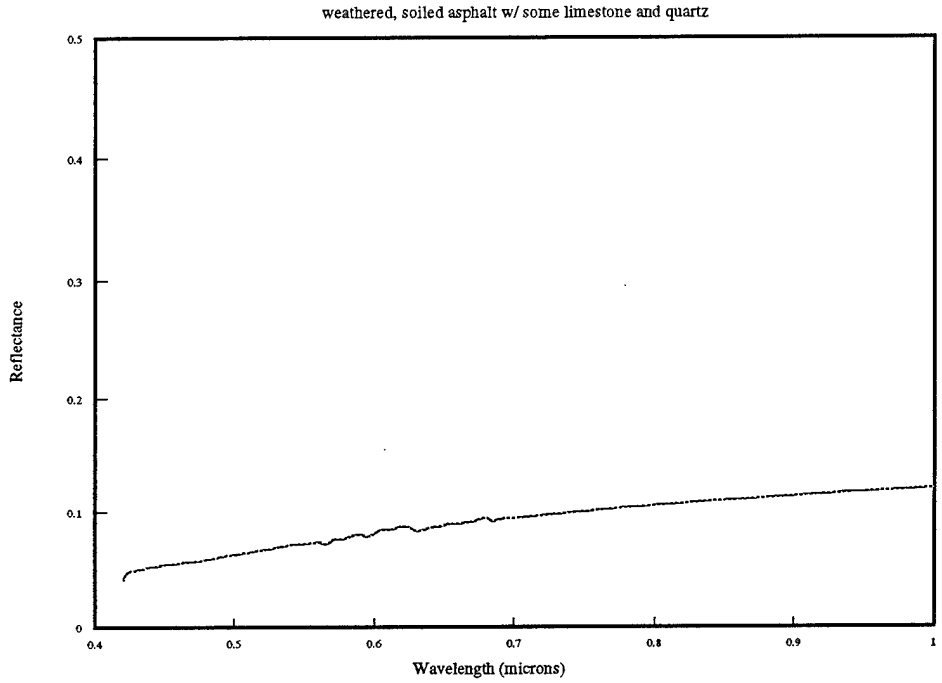

Figure 3-1. Visible and Near IR Spectrum of Weathered Asphalt

3.2 HYPERSPECTRAL

Hyperspectral systems are more typically used in the mid to far IR. The difference between hyperspectral and multispectral is the number of spectral bands which are collected for any given scene. Hyperspectral data is collected with a scanning interferometer. The interferometer types vary (difraction, Michelson, etc.) but the physics is the same. Consider a Michelson type interferometer as shown in Figure 3-3. The radiation is incident at the input aperture and is split and recombined at the beam splitter BS1. Mirror M1 is fixed while mirror M2 is scanned. The two-dimensional CCD collects an image for each mirror position x. This results in a data cube for each scan of the interferometer. Each frame is a map of intensity $I(x)$, for a particular x. The frequency spectrum for the pixel in the i^{th} row and the j^{th} column is

$$G_{i,j}(k) = \sum_{n}^{N} I_{i,j}(x_n) e^{ikx_n} . \qquad (3\text{-}1)$$

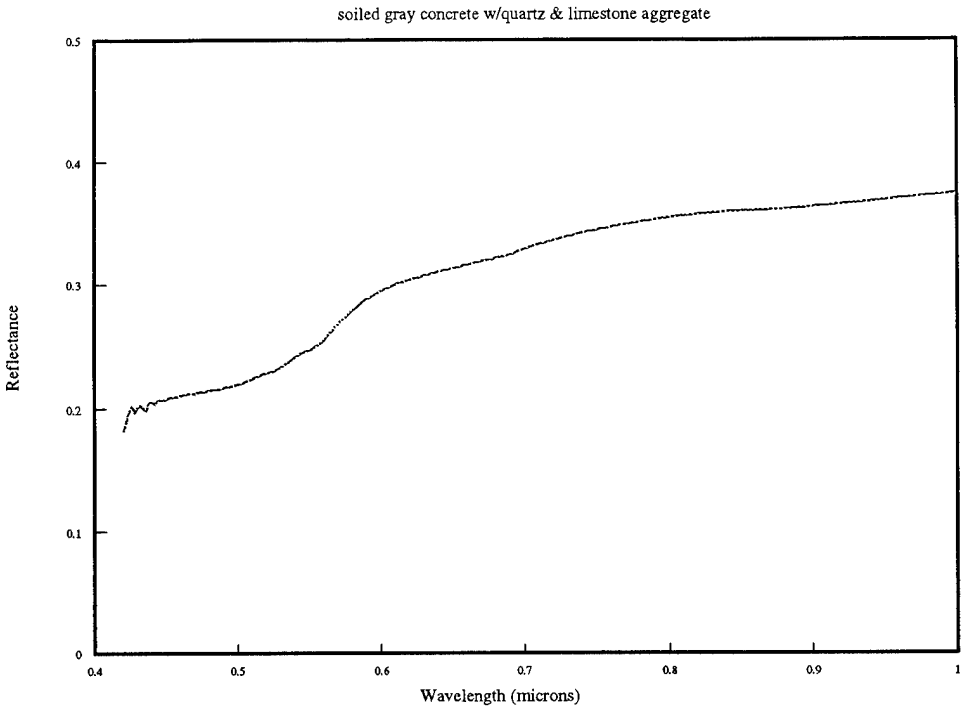

Figure 3-2. Visible and Near IR Spectrum of Weathered Concrete

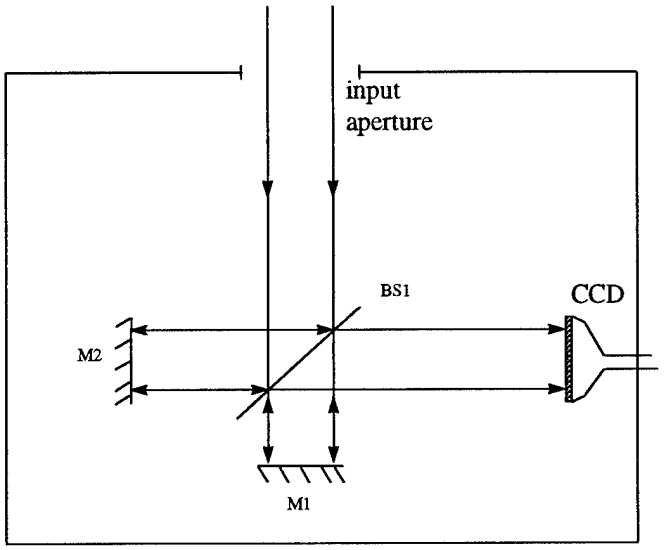

Figure 3-3. Scanning Michelson Interferometer

By using $k = 2\pi / \lambda$ and $x = ct$, the analysis can be done in frequency/time space rather than wave number/position. The sum in Equation (3-1) is evaluated for each *k* at each pixel. The data is then sorted according to wave number (or frequency). The difference in wave number between bands is

$$\Delta k = \frac{1}{N\Delta x}. \qquad (3\text{-}2)$$

Not all of the spectral bands contain useful information. Typically, some knowledge of which bands contain useful information is known a priori so that data can be quickly accessed without having to sort through every spectral band. Once the useful spectral bands have been identified, a spectral anomaly detection algorithm can be applied to the images. The approach is to examine the frames for localized spectral differences, most typically implemented by comparing differences between a pixel of interest and its nearest neighbors. This method has been successful in detecting military vehicles in cluttered backgrounds.[2]

If the spectrum of the object of interest is known in advance, a spectral matched filter algorithm can be applied to the data. Another approach, which does not require a priori knowledge of the spectral signature, is to incorporate a spectral reference library into the image processing algorithm. The algorithm then matches the spectral signatures of objects in the scene with the library contents and identifies them according to how well they match. The algorithm also identifies objects for which it has no spectral match. This method is very useful for detecting camouflage in the IR where the spectral reflectance properties result from the type of material (non-natural versus plant or mineral) rather than the color (as in the visible). A combination of these two methods, along with the thermal differences method described in the next chapter, has been used in detecting recently buried mines.[3]

This method is not particularly well-suited for detecting pavement anomalies because, as in the multispectral case, the cracks and holes will have the same spectral signature as the bulk pavement. However, patches in a runway could easily be detected with the spectral anomaly algorithm provided the patch material is different than the bulk material (concrete slurry or tar patches on asphalt, for example). Also, the material properties of the bulk pavement can be detected using this method. Silicon dioxide (SiO_2, the primary component of quartz, granite and basalt), for example, has a distinct reststrahlen (resonant absorption) doublet feature at 8-9 μm in the far IR. Calcium carbonate (the primary component in cement, dolomite, oyster shells and limestone) has a distinct reststrahlen peak at 11.2 μm. These minerals also have distinct features in the mid IR. One could use a spectral library of the basic minerals (silicon dioxide, calcium carbonate etc.) or of various rocks used as aggregate (granite, quartz, basalt, limestone etc.). The spectral signature of the pavement would then be compared with the spectral library and a list of components and percent of each component could be generated. Figures 3-4 through 3-7 (Courtesy J. Salisbury, JHU) show the mid and far IR spectra of asphalt cement, concrete cement with two different aggregates, and black tar, respectively. It is easy to pick out the quartz, carbonate and limestone features from these spectra. Figure 3-7 is featureless because tar and asphalt are similar to ideal blackbodies, reflecting very little and absorbing nearly all incident thermal radiation.

Hyperspectral data can also aid in assessing dirt landing strips. Disturbed soil, undisturbed soil and hard packed soil are easily distinguishable spectrally. Thermal images very clearly show recent tire tracks on dirt roads. Disturbed soil has a rather flat spectrum in the 3-12 μm region, while the spectrum of undisturbed soil has the features associated with the minerals present in the soil. Plants and weeds growing on the airstrip or in cracks or holes in pavement are also clearly distinguishable spectrally. Spectral differences in soft and puffy versus hard and smooth dry lake

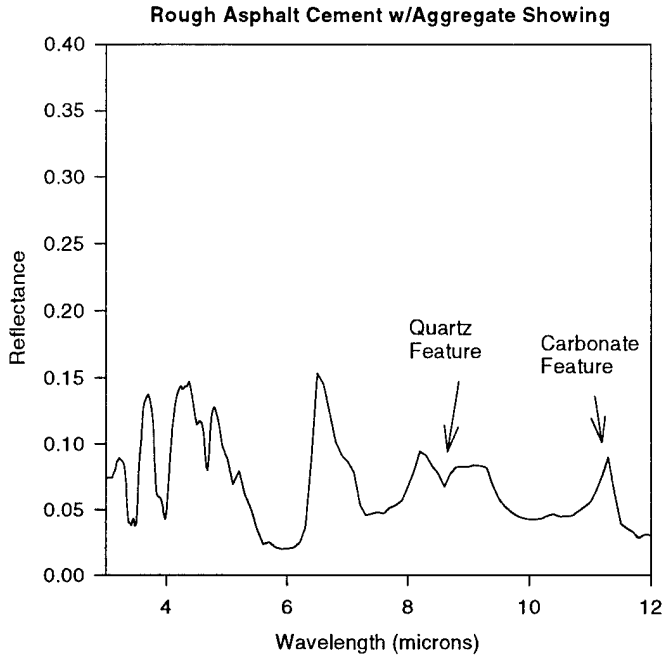

Figure 3-4. Reflectance Spectrum of Rough, Variegated Asphalt Cement in the Mid-Far IR

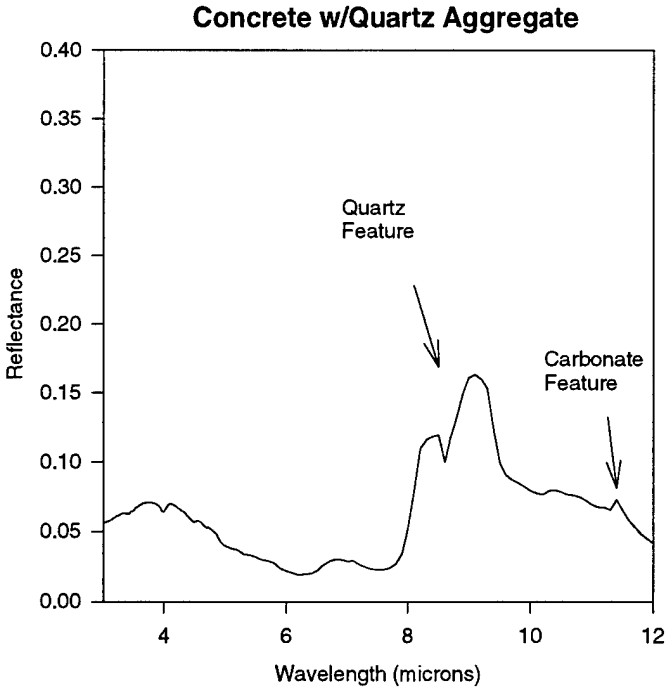

Figure 3-5. Reflectance Spectrum of Concrete Cement with Quartz Aggregate in the Mid-Far IR

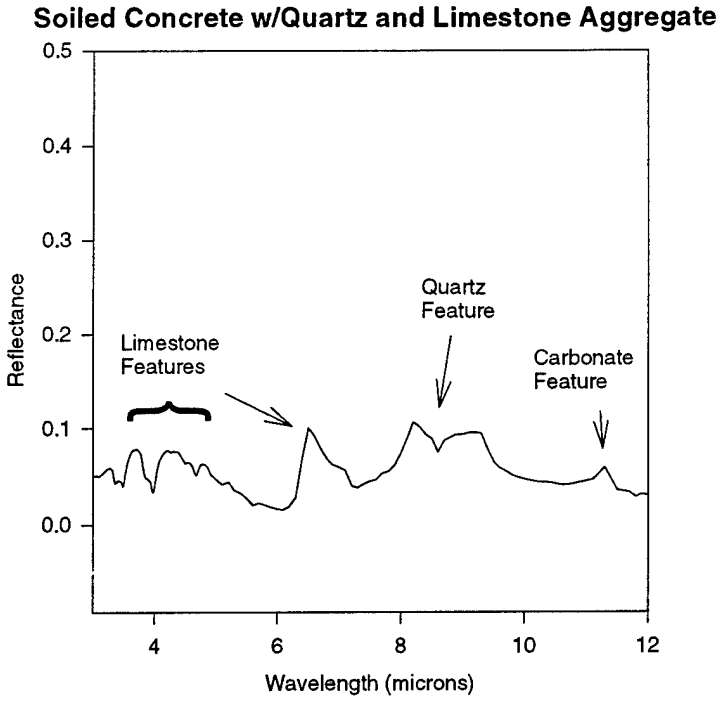

Figure 3-6. Reflectance Spectrum of Concrete Cement with Quartz and Limestone Aggregate

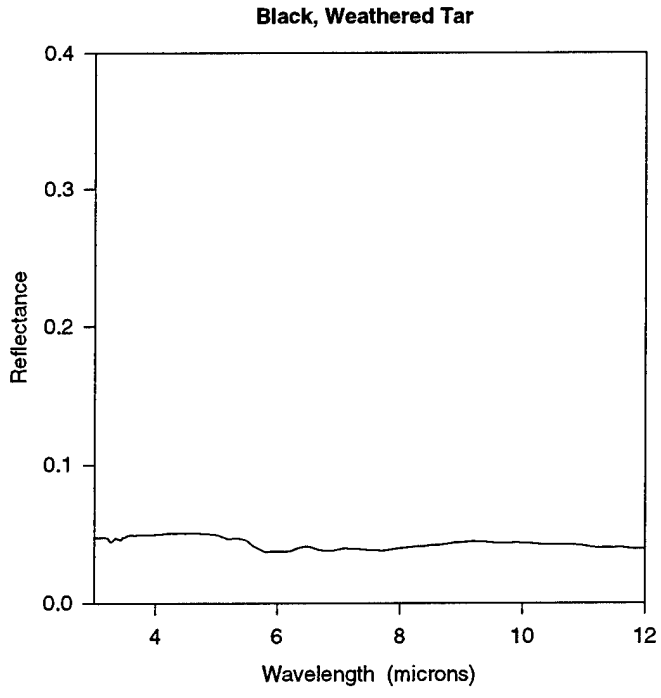

Figure 3-7. Reflectance Spectrum of Black, Weathered, Matte Tar

beds has been exploited[4] for determining the suitability of landing the space shuttle. The soft and puffy lake beds contain salts which push up the dirt and make it fluffy. The salt crystals have bound water which has strong absorption peaks at 1.66 μm and 2.2 μm. The presence of this absorption spectra in a dry lake bed in the desert indicates the presence of these salts, thus determining the unsuitability of using the area as a landing strip.

3.3 THERMAL

Electromagnetic radiation in the mid to far IR (3-12 μm) is the region of thermal blackbody radiation. The radiant exitance of a blackbody is given by

$$M_{BB}(\lambda, T) = \frac{2\pi c^2 h}{\lambda^5 (e^{\frac{hf}{kT}} - 1)}, \tag{3-3}$$

where c is the speed of light, h is Plank's constant, k is Boltzman's constant, T is the absolute temperature (in degrees Kelvin), and λ is the wavelength of the radiation. The amount of thermal energy an object will radiate depends on its emissivity. The emissivity is a material property; certain materials will absorb and re-emit more readily than others. In general, a black painted object will absorb and re-emit thermal radiation more than a white painted object. The emissivity of an object is defined relative to the emissivity of an ideal blackbody at the same temperature and wavelength, i.e.,

$$\varepsilon = \frac{M_{object}(\lambda, T)}{M_{BB}(\lambda, T)}, \tag{3-4}$$

so that the emissivity of an ideal blackbody is one. If the transmittance is zero, then conservation of energy requires that

$$a + r = 1 \tag{3-5}$$

where a is the absorption and r is the reflectance. In thermal equilibrium $\varepsilon = a$ (the body is absorbing and emitting at the same rate), in which case the emissivity can be written

$$\varepsilon = 1 - r. \tag{3-6}$$

In thermal equilibrium the emissivity, as a function of wavelength, can be obtained from the reflection spectra of the various materials in Figures 3-4 through 3-7. For black asphalt with very little aggregate, the emissivity curve is plotted in Figure 3-8. The emissivity for weathered concrete is shown in Figure 3-9. Both asphalt and concrete are good absorbers (emitters) in the thermal IR region. The emissivity of the black asphalt is very close to that of an ideal blackbody. The emissivity of tar, shown in Figure 3-10, is an even better blackbody radiator.

Infrared imaging records the surface temperature in the scene. The surface temperature is dependent on the subsurface, surface and ambient temperatures. Heat energy is transferred by

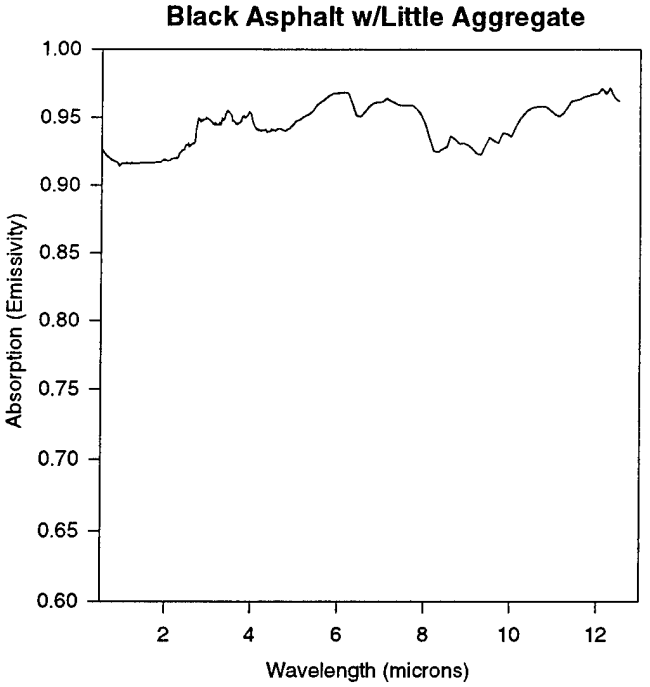

Figure 3-8. Absorption Spectrum of Black Asphalt

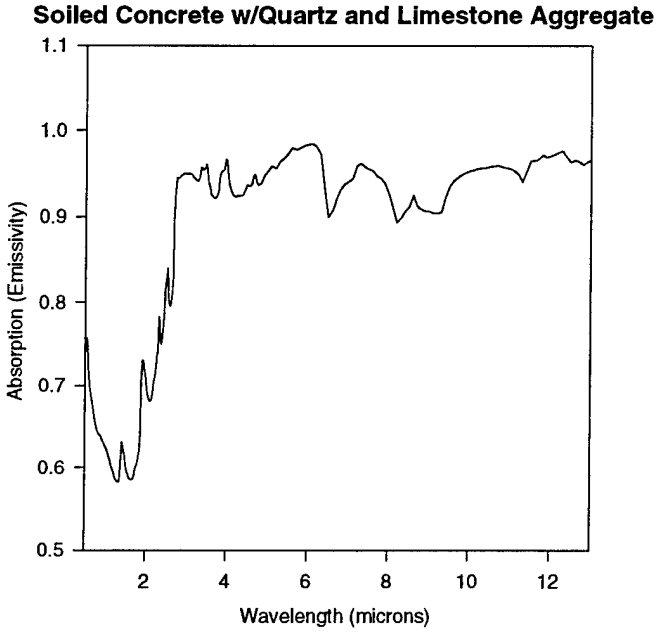

Figure 3-9. Absorption Spectrum for Concrete

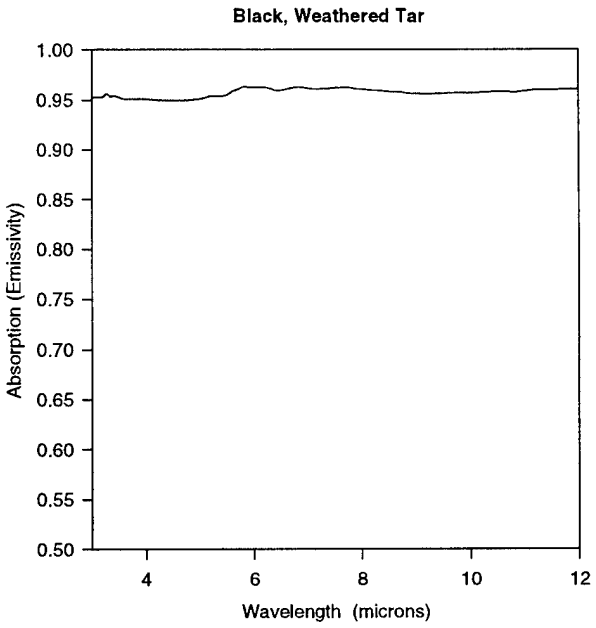

Figure 3-10. Absorption Spectrum for Black Tar

conduction, convection and radiation. The ability of the material to radiate energy is measured by the emissivity, which is strictly a surface property. In general, a rough surface will have a higher emissivity than smooth surfaces. Inspecting large areas of concrete with this method requires knowledge of surface texture, i.e., rubber tire tracks, loose sand or gravel, etc. Cracks, holes, spalls and other surface anomalies should radiate more heat than the surrounding flat surfaces because there is more surface area inside a crack or hole.

Good pavement has good heat conduction and negligible heat convection. A void beneath the surface will increase the insulation of the pavement by reducing the heat conduction without increasing the convection. The dead air space in the void does not allow for convection currents. In a thermal image the region over the void will appear to be hotter or cooler than the surrounding pavement.

Thermal imaging has been successfully used[5,6] for detecting delaminations and voids on bridges and airport runways. Successful thermal imaging requires a temperature difference between the material under inspection and the ambient background. That is, if the pavement anomalies are in thermal equilibrium with the background, they will not be distinguishable in a thermal image. Therefore a heat source and a heat sink, with temperature flow, is required. In the daytime, during periods of heating, the heat source is the sun and the pavement is the heat sink. At night, during periods of cooling, the pavement will be the source and the sky will be the heat sink. The two to three hours starting at sunrise is the best time for thermal imaging during the period of heating. The two to three hours starting at sunset is best for imaging during the period of cooling. This method works best when there is no cloud cover, since clouds reflect IR radiation. High gusts of wind have a cooling effect on the surface, therefore testing should not be

done when wind speeds are high. Finally, testing should not be performed when there is standing water on the surface. Water is a strong absorber in the IR and acts like a mask.

3.4 STEREOSCOPIC

Stereoscopic imaging is a technique that employs two cameras for measuring distances to a high degree of accuracy. Of all the techniques presented in this chapter (passive imaging), stereoscopic imaging is the only one that yields information about the surface roughness or the depth of cracks, holes, spalls and trenches. This information is necessary to assign a pavement condition index.

Two detectors are separated by known distance *d*, as shown in Figure 3-11, and the look angles θ and φ are known. When a point on the surface is in the FOV of both detectors, the height *h*, between the detectors and that point can be calculated in the following way. The angle between the two detectors is given by

$$\zeta = 180 - \theta - \varphi . \tag{3-7}$$

By the law of sines,

$$A = d\frac{\sin\varphi}{\sin\zeta}, \tag{3-8}$$

and

$$h = A\sin\theta = d\frac{\sin\varphi}{\sin\zeta}\sin\theta . \tag{3-9}$$

The accuracy of *h* depends on the accuracy's of *d*, θ, and φ. The two detectors in Figure 3-11 can be synchronously scanned across the surface to obtain the heights along the x-direction, while the forward motion of the platform gives the heights along the y-direction for subsequent scans. A three dimensional map of the surface can then be reconstructed. Alternatively, two CCD cameras with overlapping FOVs can be used. The angles and distances between pixels must then be known on a pixel-by-pixel basis.

This method is particularly useful for determining the severity of trenches and the overall evenness of the surface. Stereoscopic imaging could also be incorporated into a thermal scanner to determine the depth of subsurface voids. Further, discrimination between surface and subsurface anomalies in thermal images can be achieved with this technique.

3.5 POLARIMETRY

Radiation from the sun is randomly polarized. When randomly polarized radiation is incident on a surface, certain polarizations will be preferentially reflected while others will be preferentially transmitted or absorbed according to Fresnel's equations. The component of

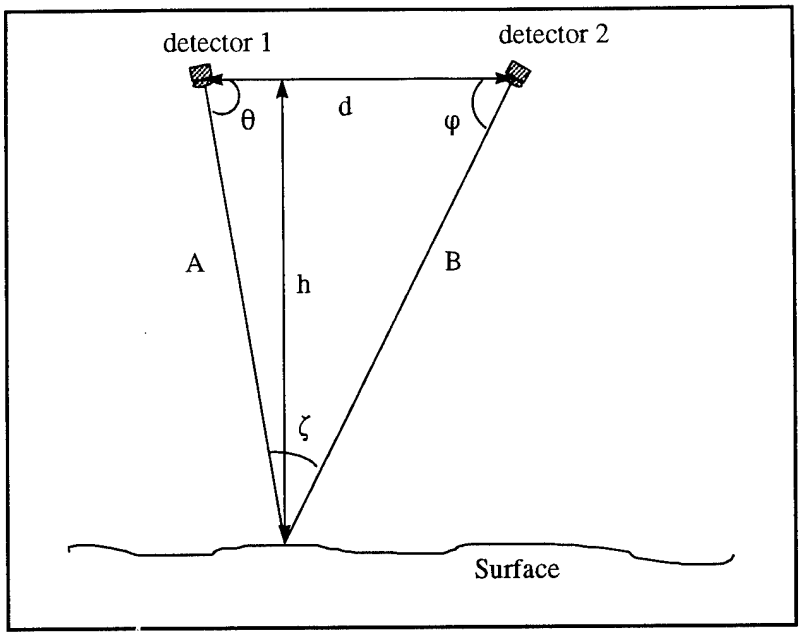

Figure 3-11. Stereoscopic Geometry

polarization that is perpendicular to the plane of incidence, defined in Figure 3-12, will have a higher reflectance than the parallel component. This very bright, polarized return is called specular reflection. It is responsible for the glare that polarized sunglasses are designed to reduce. Specular reflection from the sun is generally polarized in the horizontal plane, therefore the axis of polarization of the sunglasses is vertical to block the glare. This effect is exploited in imaging systems by mounting a polarizer, with the polarization axis horizontal, at the camera input. This will enhance detection of specular reflections. This technique is particularly useful for mine hunting applications because metal surfaces generally have a high specular return whereas the background (earth, sand, vegetation) does not.

For application to remote sensing of airstrips this method may aid in detecting surface anomalies. Any sharp edges or corners may induce specular reflections depending on the look angle with respect to the angle of incidence of the sunlight. Most pavements do not induce specular reflections in the visible, but there may be some in the reflected portion of the thermal IR.

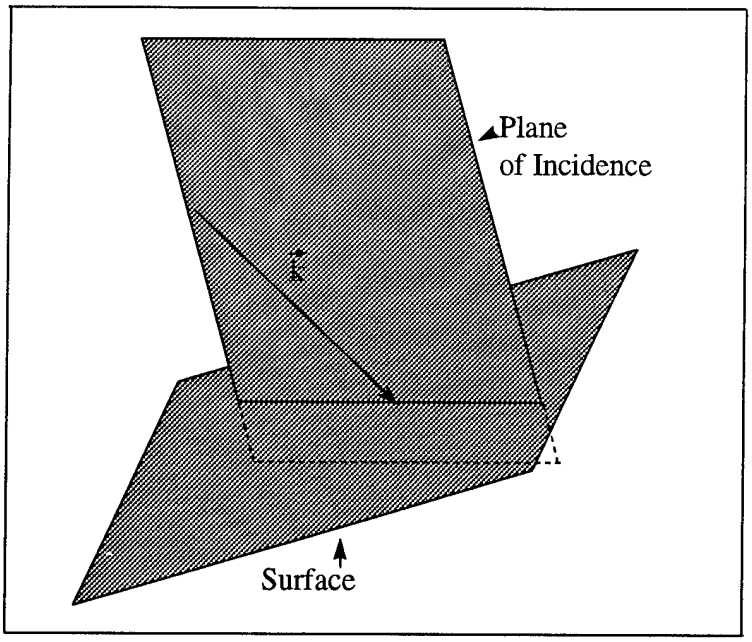

Figure 3-12. Geometry for Plane of Incidence (**k** is the momentum vector of the incident radiation)

CHAPTER 4

ACTIVE IMAGING SYSTEMS

Active imaging systems require a light source, most typically a laser. Incorporating a light source into the imaging system increases the expense, difficulty of implementation and operation and should not be considered unless there is a compelling reason (significant increase in detectability). Active imaging systems are ordinarily employed for detecting objects embedded in turbid media (moored mines in ocean water, for example). Employing a laser source when imaging through turbid media significantly improves signal-to-noise and target detectability. Active imaging can be employed at any wavelength, ultraviolet to IR, so long as a laser or light source can be found at the desired wavelength. This discussion is therefore applicable to all the thermal and visible techniques discussed in Chapter 3. However, the multispectral technique would require a frequency agile laser (able to switch frequency output for each input filter), which does not currently exist.

For the purpose of remote airfield assessment, LIght Detection And Ranging (LIDAR) imaging systems are not necessary, nor are they recommended. Except in conditions of poor visibility, such as thick fog or smoke, passive imaging through the atmosphere is nearly as effective. This is true for LIDAR systems that do not give depth information. In typical LIDAR systems, the beam is expanded and a two dimensional CCD is used as the detector. The result is a two dimensional map of intensity versus x-y positon. Two types of LIDAR systems which do yield depth information are the pulsed, scanning LIDAR and the beam fanning LIDAR. These systems yield information about the surface structure that, in passive systems, only the stereoscopic technique can achieve (Chapter 3.4). The details for the scanning and the beam fanning LIDAR are presented this chapter.

4.1 SCANNING LIDAR

The line scan system has been applied to both active and passive imaging systems. For active systems, either a continuous or a pulsed laser is used. If height information is required, a pulsed laser must be used. The narrow, pulsed beam is scanned along the x-direction, usually with a rotating mirror assembly. A second mirror in the scanning assembly collects the return signal and reflects it into a single detector, usually a photomultiplier tube. The forward motion of the platform yields the y-axis information for subsequent scans. In this way a two dimensional image can be constructed. For a pulsed laser system, the height information is obtained by measuring the time between the launch of the laser pulse and the return signal. This time of flight of the laser pulse corresponds to twice the distance from the LIDAR system to surface of reflection; i.e., $2h = c\,\Delta t$, where c is the speed of light in air. The height information can be

obtained on a pixel-by-pixel basis throughout the scan and a three dimensional map of the surface can be constructed.

The vertical resolution is limited by the rise time of the detector. Current state-of-the-art photomultiplier tubes have rise times of ~0.5 ns. This corresponds to a vertical resolution of 15 cm (or 0.5 ft). State-of-the-art avalanche photodiodes have a rise time of ~150 ps, corresponding to a resolution of 4.5 cm (~ 2 in.). These photodiodes have triple the resolution however they also have less gain and dynamic range than the photomultipliers. These resolutions can be nominally improved by leading edge detection techniques. One researcher[7] achieved a resolution of 2 mm in a thermal scanning system by modulating the laser source. However, maintaining the millimeter resolution would be technically difficult if the system were to be integrated on an airborne platform, and would probably result in imposing serious limits on the speed and height of the platform.

The resolution in the y-direction (the direction of motion of the platform) will be determined by the speed of the platform and the scan rate. Since the scan rates are matched with the platform velocity to maintain a uniform pixel size (width equals length), these factors will also determine the resolution in the scan direction (x-direction). Typical scan rates are 0.5-4.0 KHz. For a platform moving at 180 kn (121.6 m/s) and a scan rate of 4 KHz, the resolution is 3 cm/line in the y-direction. If the readout rate is set at 1024 measurements/scan (or pixels/scan) then the FOV in the x-direction is 31 m (102 ft). This requires a readout rate of 4 MHz, which is within the capability of a photomultiplier tube in a continuous line scanner (timing cannot be measured), but it may be difficult to implement for the range requirements of the pulsed LIDAR (timing measurements for height information on each readout). Furthermore, the laser pulse repetition rate must be matched to the readout rate imposing an additional requirement on the system. The pulse repetition rate must also be variable to allow for adjustments in readout rates based on changes in platform velocity.

All of these requirements are possible, however they would be extremely difficult to implement on an airborne platform. With the high readout rates it may be necessary to sacrifice intensity information in each pixel; i.e., it may not be possible to measure both range (by timing) and intensity (integration over return pulse) at high speed. A change in platform height would be translated into a change in the surface structure unless a correction mechanism is built in to the acquisition system. Furthermore, all parameters must be continuously adjustable. For resolutions of 0.5 ft, it hardly seems worthwhile.

4.2 BEAM FANNING

Beam fanning is an active imaging technique using a continuous laser source. The beam is expanded in one direction, by means of a cylindrical lens, so it looks like a fan. The detector is a one dimensional diode array (or CCD). This system does not require scanning; the diode array detects the laser return providing the x-axis information while the forward motion of the platform gives the y-axis for subsequent readouts of the array. In this way a two dimensional image of intensity versus x-y position can be constructed.

Used in this way, beam fanning does not provide depth, or surface structure information. However, if a two dimensional CCD is used, instead of a linear array, and there is a separation *d*, between the source and receiver, then surface structure can be obtained. This is similar to the stereoscopic method outlined in Chapter 3.4 (compare to Figure 3-11). The configuration for this technique is shown in Figure 4-1. The surface has an exaggerated step of height h_2, for illustrative purposes. If the surface was perfectly flat, $h_2 = 0$, and the camera would record a straight line of illuminated pixels. For the surface shown in Figure 4-1, the camera "sees" a step of apparent height h_{app}. In this configuration the fan beam is coincident with the z-axis so that $\varphi = 90°$. Equation (3-9) then reduces to

$$h = d\frac{\sin\theta}{\sin\zeta} = d\tan\theta. \qquad (4\text{-}1)$$

The distance *d*, from the laser source to the row of pixels illuminated by the portion of the line from point A to point B, along with the look angle θ, are used in Equation (4-1) to calculate h_1. The portion of the line from point C to point D illuminates a different row of pixels. The distance from the laser source to the new row of pixels is used in Equation (4-1) to calculate $h = h_1 + h_2$. Alternatively, h_2 can be calculated from

$$\zeta = 90 - \theta, \qquad (4\text{-}2)$$

and

$$h_2 = \frac{h_{app}}{\sin\zeta}, \qquad (4\text{-}3)$$

where h_{app} is calculated from Equation (2-3) by multiplying x_{pix} by the number of pixels illuminated by h_{app} at the CCD. When $\zeta = 0$, $h_{app} = 0$ also. Thus, when the source and receiver are colinear (d=0) all height information is lost. When $\zeta = 90°$, $h_2 = h_{app}$. As in the stereoscopic imaging case, the accuracy (resolution) with which *h* can be measured will depend on the accuracy that the source-receiver separation and the angles are known.

In this configuration, the fan beam system will measure longitudinal non-uniformities along the direction of motion of the platform. The frame rate of the CCD would have to be very fast since only one line at a time is actually recorded per frame. The fastest frame rate for CCD cameras is about 1000 frames/s. At a platform velocity of 121.6 m/s (180 kn), the resolution is 12 cm/frame (~5 in./frame).

To measure non-uniformities in the surface transverse to the direction of motion a second beam would have to be incorporated to scan in the x-direction. This involves incorporating scan rates with frame rates and the associated difficulties discussed in the previous chapter.

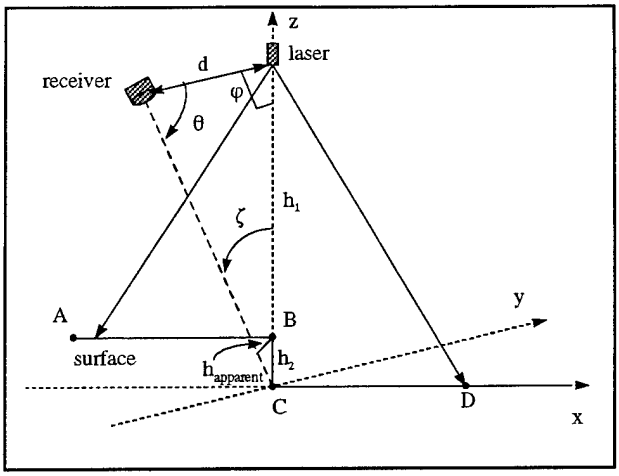

Figure 4-1. Diagram of Beam Fanning System for Measuring Surface Roughness

CHAPTER 5

FIELD TEST RESULTS

During the week of September 10, 1996, a field test was performed at Wright Laboratory, Tyndall Air Force Base (TAFB), FL. The test was performed by Dr. Nancy Swanson of the Naval Surface Warfare Center, Dahlgren Division (NSWCDD), Hugh Welker of Applied Research Associates, and Brad Blume of Nichols Research Corporation. The purpose of the test was to gather images, in multiple spectral bands, of certain areas of the test runway at Wright Laboratory (visible and IR) to aid in the study of the application to remote airfield assessment.

There were two cameras used in this test; one sensitive in the visible portion of the electromagnetic spectrum (400-700 nm) and the other sensitive in the IR from 3-12 μm. Areas of the test runway were first marked out in grids. The areas were chosen to incorporate a variety of pavement conditions to assess the capability of detection for each condition in each spectral band. The areas were labeled with letters from A to M. Each area was measured and the cracks, faults, holes, patched craters and spalls, and voids inside the area were measured and recorded. Areas A-C were located in the flexible test section (sand subgrade, 18 in. sand fill, 12 in. crushed Alabama limestone basecourse, and 6 in. asphalt) with the gyratory asphalt mix. Areas D-G were in the composite test section (sand subgrade, 6 in. seashell, 10 in. limestone basecourse, 12 in. Portland cement, and 6 in. asphalt) with the gyratory asphalt mix. Areas H-J were in the composite test section with the Marshall asphalt mix. Areas K and L were in the flexible test section with 6 in. of Marshall mix asphalt. Area M was in the flexible test section with 4 in. of Marshall mix asphalt. All the craters were patched with ASR-1 magnesium phosphate slurry with no. 4 Alabama crushed limestone. All the spalls were patched with just the magnesium phosphate slurry.

5.1 VISIBLE IMAGES

The visible camera was a MTI 72 series CCD camera with 768(H)X493(V) active pixel elements. The horizontal dimension of the pixels was 11 μm and the vertical was 13 μm. There were two lenses used throughout the test, 16 mm and 12.5 mm. The height of the camera from the surface of the pavement was 21.25 ft (6.5 m). The viewing angle was approximately 20°, though this varied slightly from one area to another. The viewing angle affects only the vertical dimension of the FOV. The FOV was 11.3(H)X9.1(V) ft^2 for the 16 mm lens and 14.4(H)X11.6(V) for the 12.5 mm lens. The resolution was 0.18 in.(4.5 mm) in the horizontal direction and 0.22 in.(5.6 mm) in the vertical direction when using the 16 mm lens. For the 12.5 mm lens, the resolution was 0.23 in.(5.7 mm) horizontal and 0.28 in.(7.2 mm) vertical. Areas A-M were imaged with the CCD camera for seven filters: 400, 450, 500, 550, 600, 650, and 700 nm, all with 80 nm bandwidth except for the 550 nm filter, which had a bandwidth of

60 nm. The spectral response of the camera (Figure 5-1) peaks at 580 nm. We found that the 550 nm filter gave the sharpest, clearest image while the 400 and 700 nm filters yielded the poorest images. This is obviously due to the spectral response of the camera since the reflectivity spectra of asphalt and concrete are relatively flat in the region from 400-700 nm, as shown in Figures 3-1 and 3-2 respectively. Concrete has a higher overall reflectivity than asphalt because it is much lighter in color. Figures 5-2 through 5-14 are images of Areas A-M taken with the CCD camera.

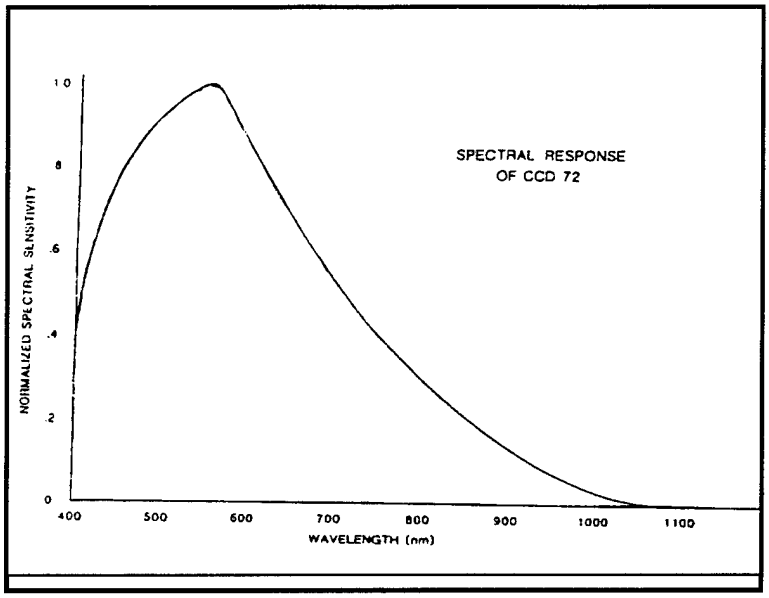

Figure 5-1. Spectral Response of CCD Camera

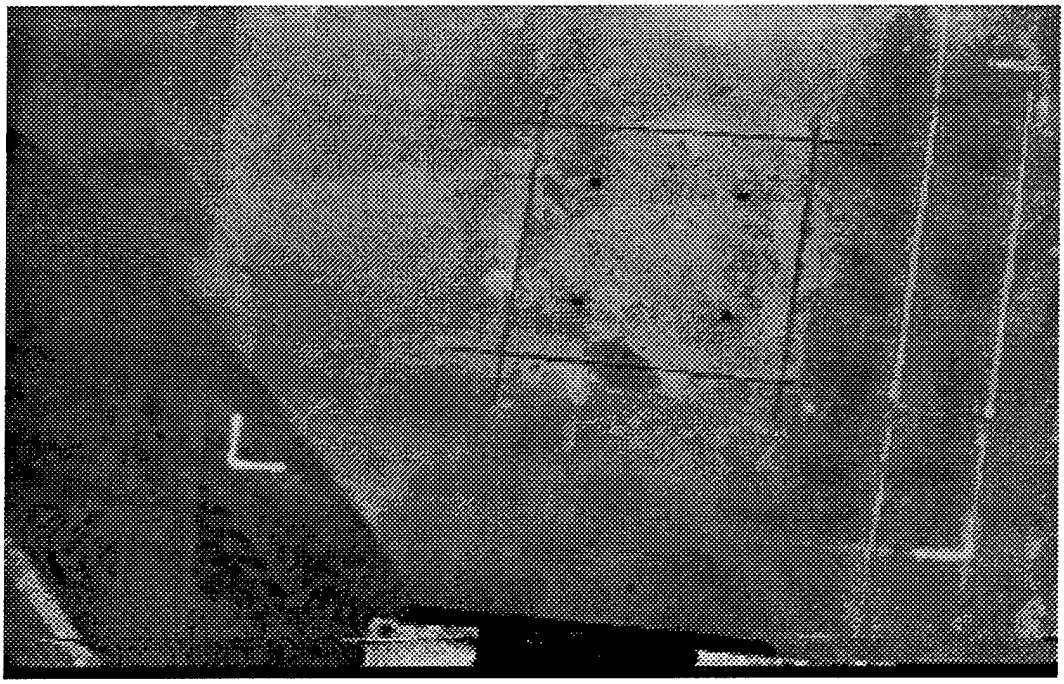

Figure 5-2. Visible Image of Area A: a 7.5 ft (W) by 6 ft (H) grid. Inside, a 2.8 ft by 2.8 ft square was cut from the 6 in. thick asphalt and lifted. A round, 2 ft diameter, 6 in. deep hole was dug under the asphalt and the square was replaced. The 1/8 in. cracks and the 1 in. bolt holes were filled with tar. On the second morning of the test the grid was painted black. This image was taken with the 650 nm filter and the 16 mm lens.

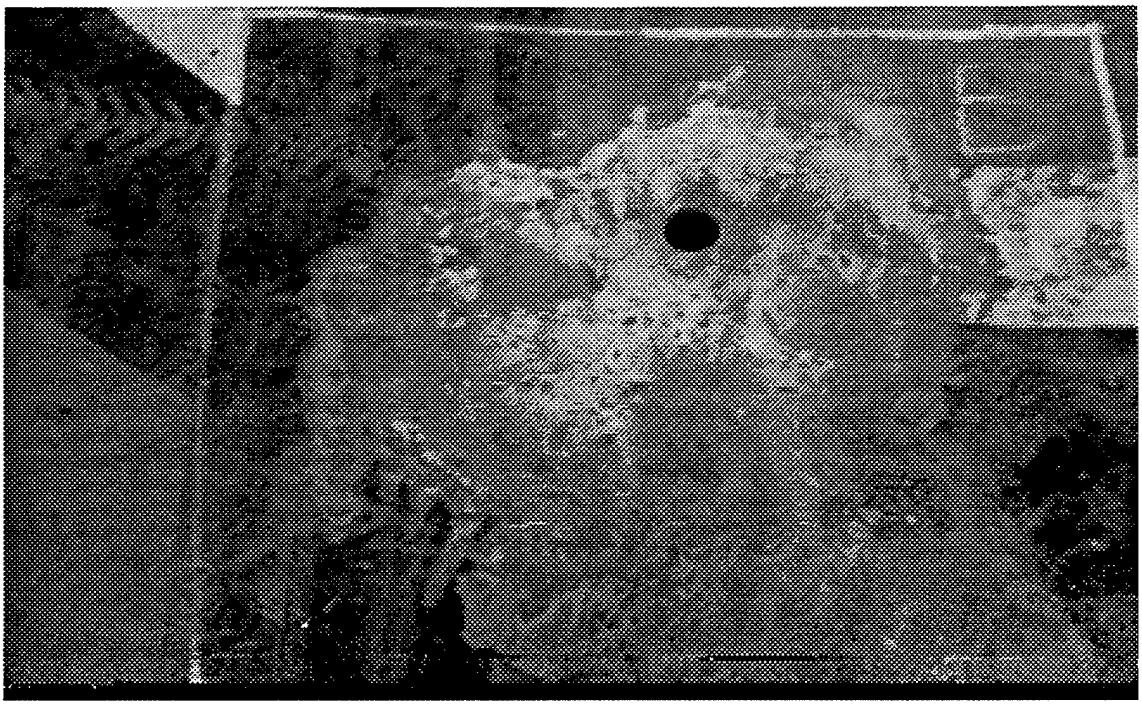

Figure 5-3. Visible Image of Area B: an 8.8 ft (W) by 8.3 ft (H) grid. The main feature is a 5 ft diameter by 18 in. deep crater with a 6.5 in. diameter, 16.8 in. deep core hole taken 8 in. off crater center. There is a wide, white paint stripe in the upper right corner just below the "B". There is aggregate showing throughout the patch and small alligator cracks in the spilled slurry at the bottom of the grid. At the lower right edge is some scaling of the patch material. This image was taken with the 650 nm filter and the 16 mm lens.

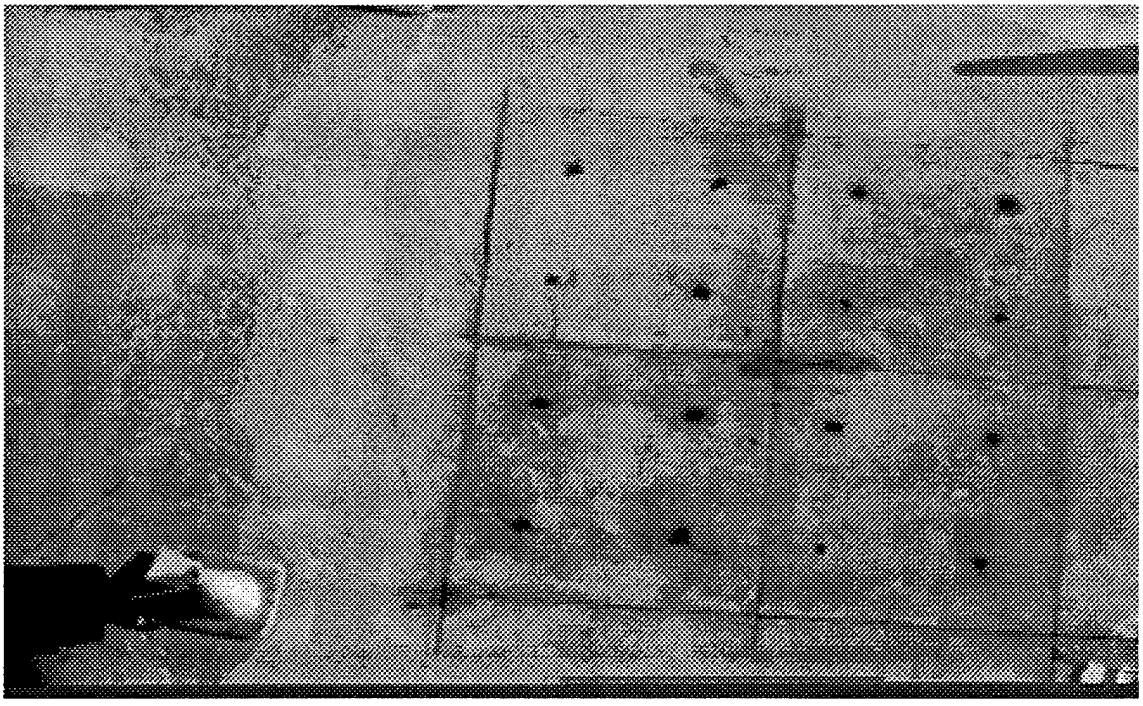

Figure 5-4. Visible Image of Area C: a 10.2 (W) by 10.2 (H) ft grid. This is similar to Area A except that four 2.8 ft by 2.8 ft squares were cut and lifted out and a 6 in. deep, 4 ft diameter hole was dug. The squares were replaced and the cracks and bolt holes were filled with tar. On the second day of testing, the entire area was painted black. Filter: 650 nm; lens: 16 mm.

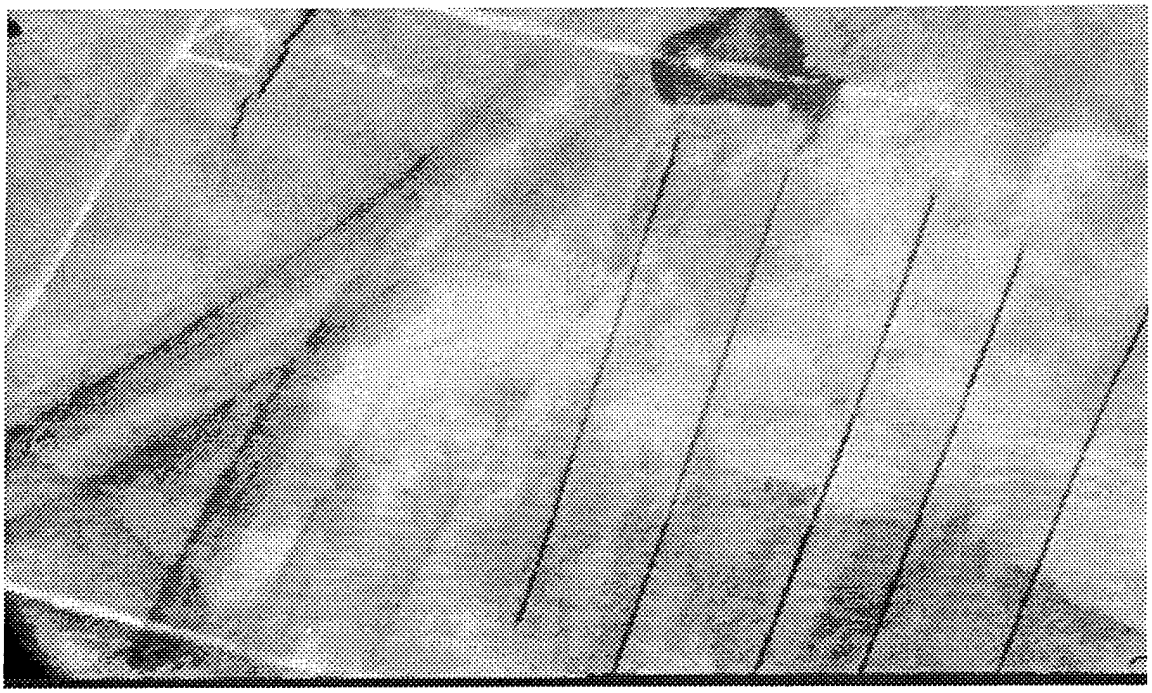

Figure 5-5. Visible Image of Area D: 8.5 ft by 12.5 ft grid. There is a large crack, approximately 2.5 ft long and 0.5 to 1.0 in. wide, just under the "D" at the upper corner of the grid. The other cracks were cut into the asphalt and from the right are: 3/8, ¾, 5/4, 3, and 5 1/8 in. in depth. They were all 1/8 to ¼ in. wide. Filter: 650 nm; lens: 16 mm. The dark spot at the top of the frame is water. The darker areas in the image are bare pavement and the lighter areas are ground in dirt.

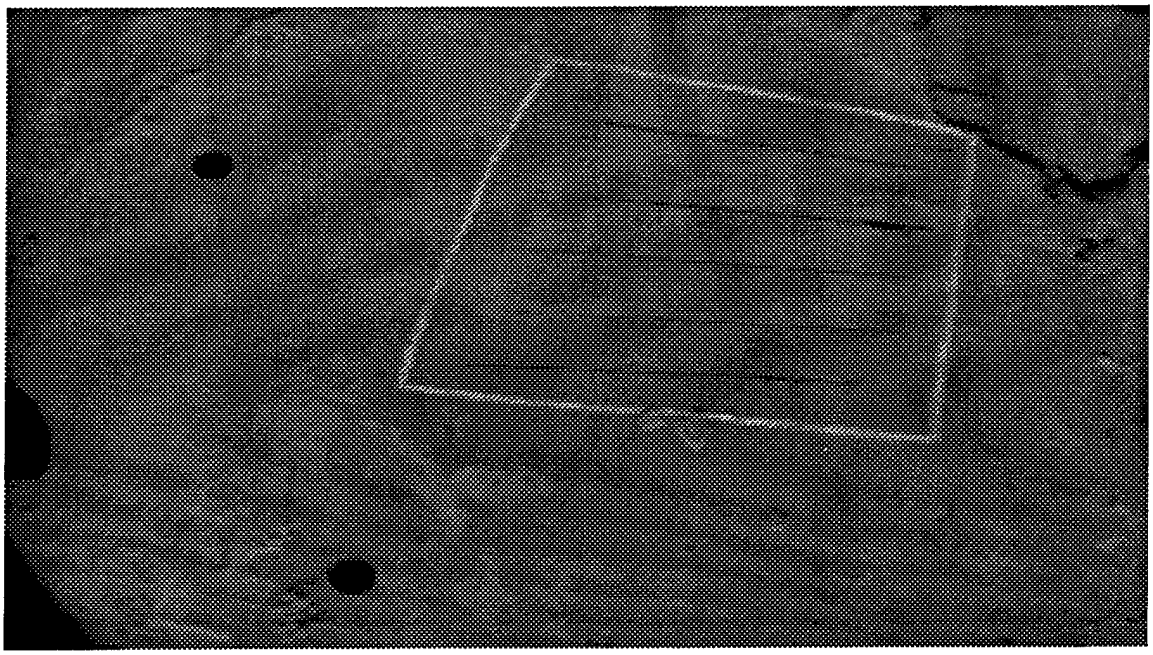

Figure 5-6. Visible Image of Area E: 10.5 ft (W) by 12.5 ft (H) grid. This grid is entirely inside a 20 ft diameter, 18 in. deep patched crater. In the lower left corner is a 6.5 in. diameter, 16.5 in. deep core hole with 1 ft of standing water. There is a ridge intruding in the upper right corner that is 1-1.5 in. higher. The five cracks were cut into the patch material. From the top they are 5/8, 9/8, 3, 5.5, and 5/4 in. deep and 1/8-3/8 in. wide. The core hole to the left was not inside the grid but was 6.5 in. diameter and 19 in. deep. Filter: 550 nm; lens: 12.5 mm.

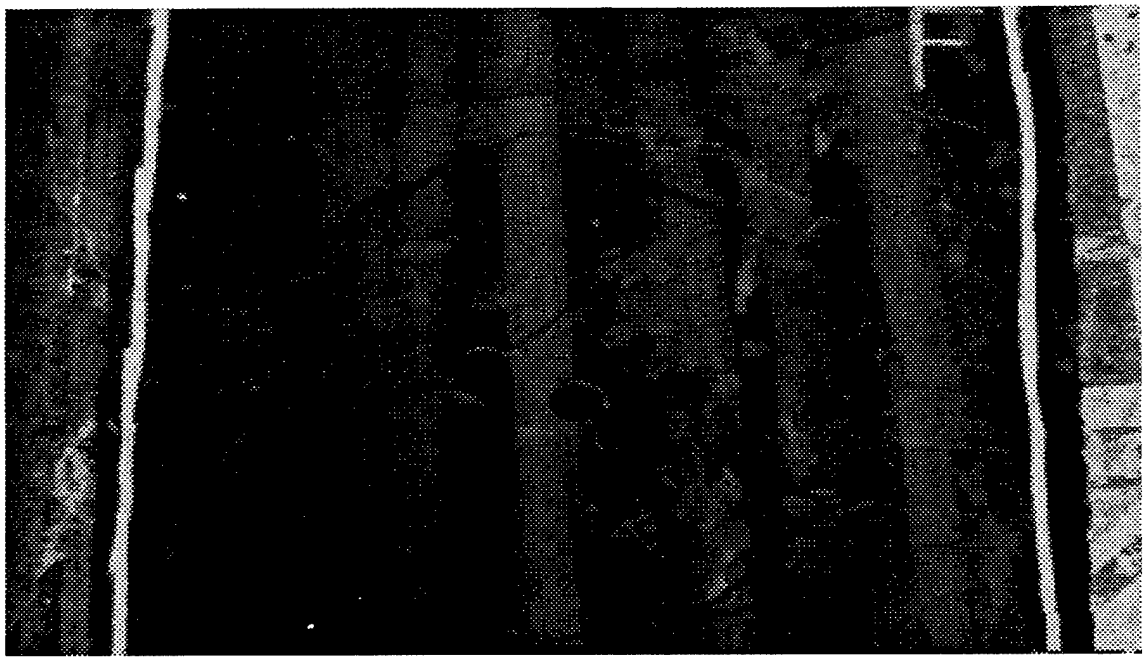

Figure 5-7. Visible Image of Area F: an 8.8 ft (W) by 10.3 ft grid. This grid has a 5 ft diameter, 18 in. deep patched crater in the center. The entire grid has been painted black. There is a 6.5 in. diameter, 17 in. deep core hole in the center of the crater. There are numerous hairline cracks and uneven areas that are not apparent in the visible images but are in the thermal. Filter: 650 nm; lens: 16 mm.

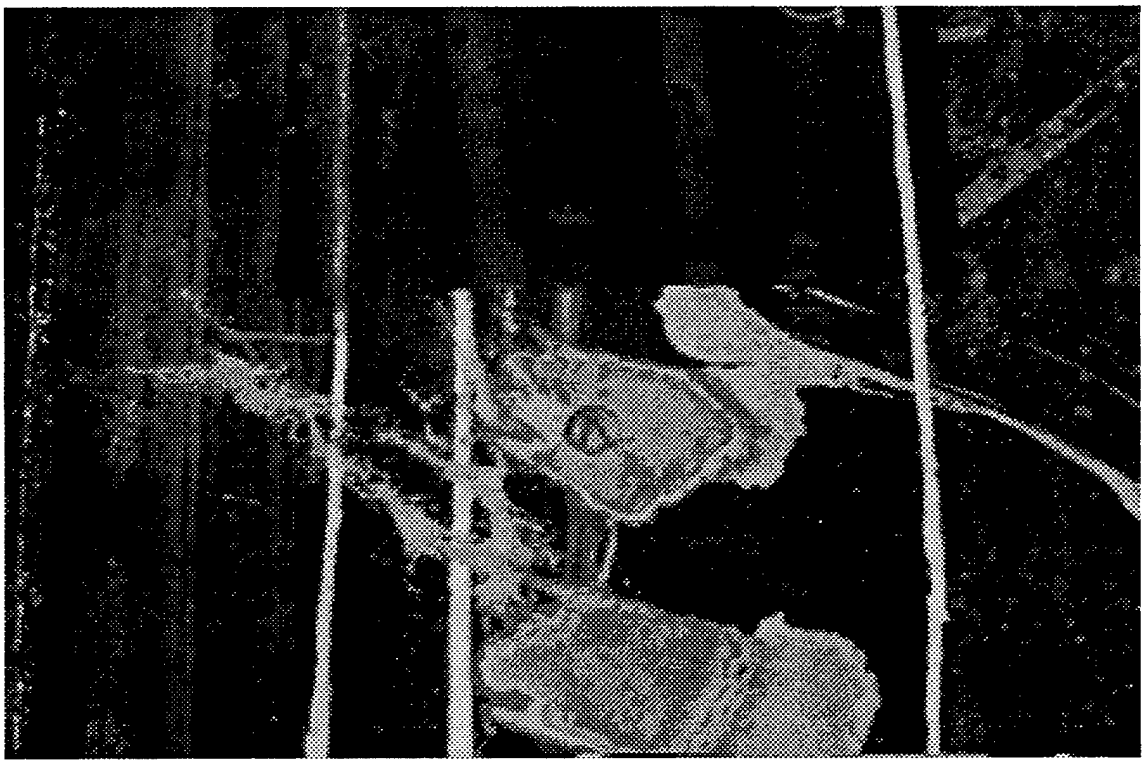

Figure 5-8. Visible Image of Area G: a 5.7 ft by 10.3 ft grid. This grid has four 1.5 ft diameter, 3-5 in. deep patched spalls. The upper half of the grid has been painted black. In the center of the second patch (from the bottom) is a 6.5 in. core hole with the 6 in., cracked core in the hole. There is a 3 in. vertical white paint strip to the left of the patches and much spilled slurry. Filter: 650 nm; lens: 16 mm.

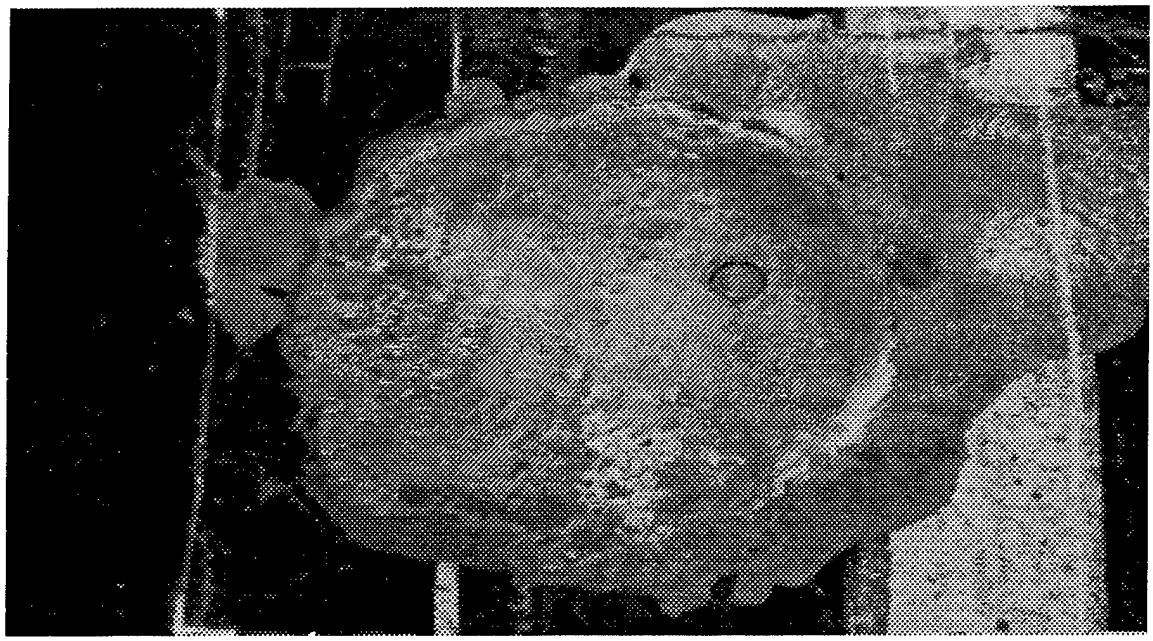

Figure 5-9. Visible Image of Area H: an 8.3 ft (W) by 8.8 ft grid with a 5 ft diameter, 18 in. deep patched crater in the center. At 6 in. off crater center is a 6.5 in. diameter, 16 in. deep core hole with the 6 in. core left in the hole. There is much aggregate showing at the bottom and left side of the patch. There are also many small cracks in the upper right surface of the patch. Across the top of the grid is a 1/8 to ¼ in. wide, 1 in. deep crack. There is much spilled slurry and two white, painted stripes. Filter: 650 nm; lens: 16 mm.

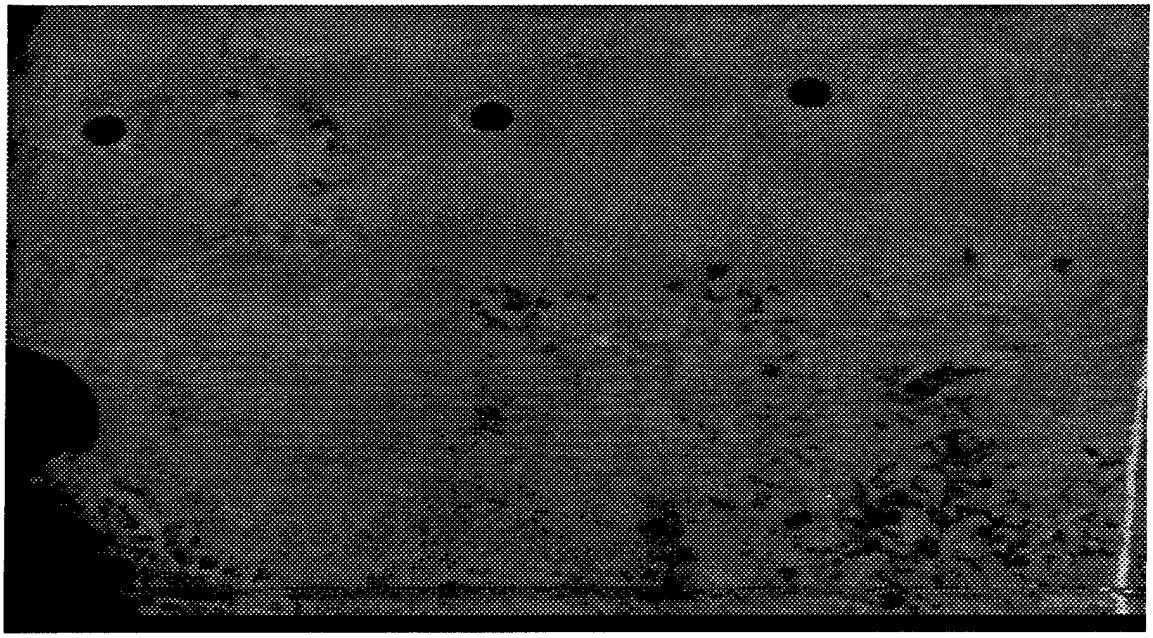

Figure 5-10. Visible Image of Area I: a 14.8 ft (W) by 14.8 ft grid inside a 20 ft diameter, 18 in. deep patched crater. The 6.5 in. diameter core holes are, from right to left, 20, 20, and 17 in. deep. The third hole has 5 in. of standing water. The first hole on the right is at the center of the crater. Not shown in this image, at the upper left edge of the patch is another core hole with the core in it. In the lower left corner is a large area of slurry that is ¼ in. higher than the rest of the patch. There are numerous hairline cracks in the surface. Filter: 650 nm; lens: 12.5 mm.

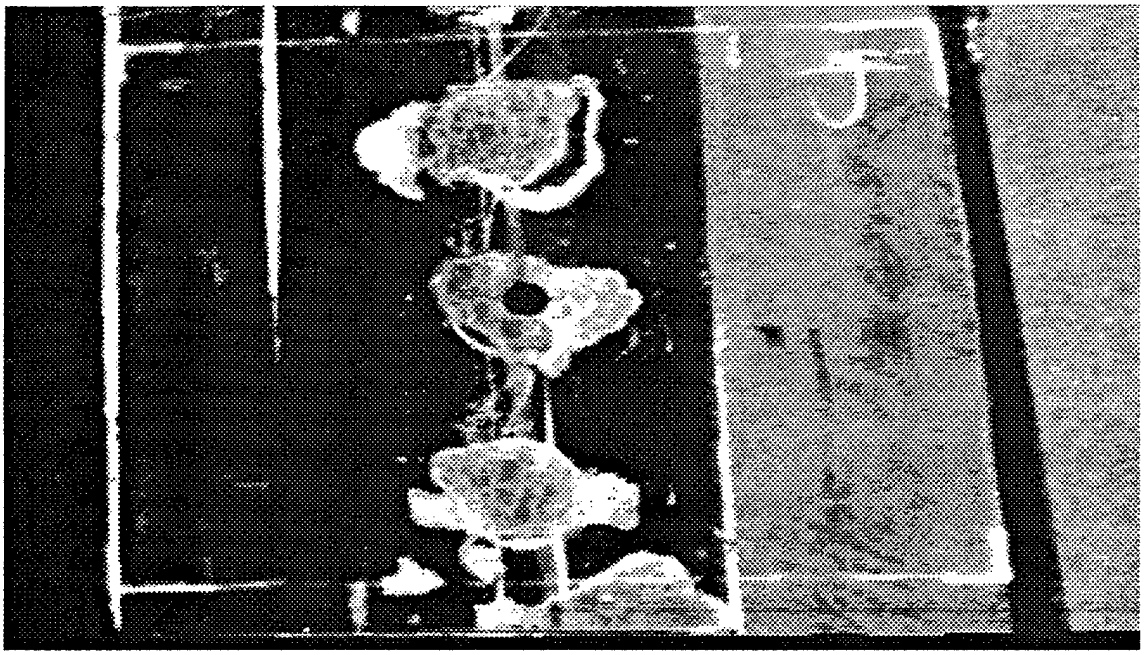

Figure 5-11. Visible Image of Area J: a 10.3 ft (W) by 9 ft grid with three, 1.5 ft diameter, 3 to 5 in. deep patched spalls. The center spall has a 6.5 in. diameter core hole filled with rocks and shells. Not visible in this image, in the lower left corner is a 3.5 in. diameter, 5.5 in. deep core hole. The right edge of the grid is painted gray, the left is painted black with three strips of white paint. There are numerous alligator cracks in the patches and spilled slurry. Filter: 650 nm; lens: 12.5 mm.

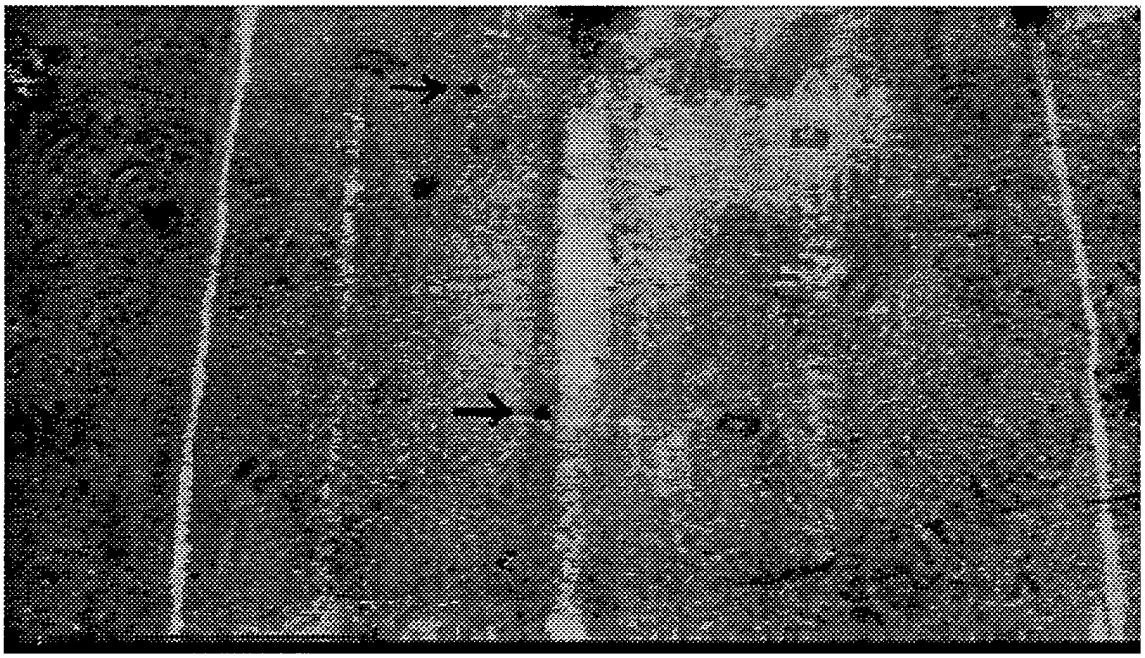

Figure 5-12. Visible Image of Area L: a 9.4 ft (W) by 20 ft rectangle with a 1.2 ft wide, 1.5 in. deep rut running the length of the grid. At the left edge of the rut toward the bottom of the image (lower arrow) is a 1.5 in. diameter, 7 in. deep bolt hole. Toward the top of the image, left of the rut (upper arrow) is another 1.5 in. diameter, 10 in. deep bolt hole. At the very top of the rut is a weed growing in the center of the rut. There is dirt in the bottom of the rut 2 ft on either side of the weed. Just above and to the left of the weed is a 4 in. diameter, ¼ in. deep hole and to the left of that is a 1.5 in. diameter, 11 in. deep bolt hole. These last two are outside the top of the frame. At the top right, on the chalk line, is another, smaller weed. Filter: 650 nm; lens: 16 mm.

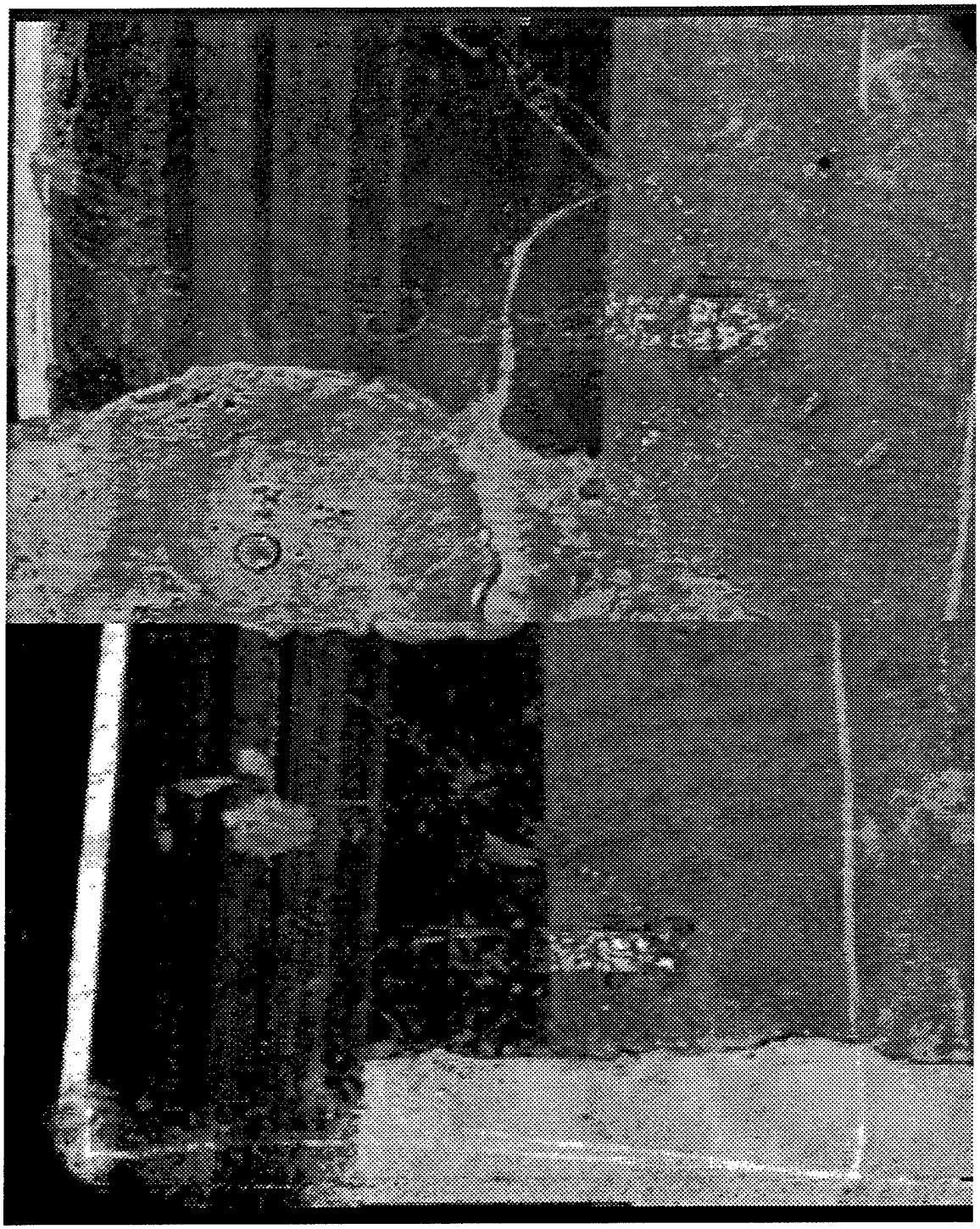

Figure 5-13. Visible Image of Upper and Lower Sections of Area K. The entire area is 10.5 ft (W) by 20 ft long. The upper image was taken with the 16 mm lens and the lower with the 12.5 mm lens. In the upper left corner is a 5 ft diameter, 18 in. deep crater with a 6 in. core in a 6.5 in. hole at the center of the crater. The left side of the grid is painted black. There are numerous old paint stripes that are nearly worn off. At the bottom right of the grid is a 2 ft wide by 7.5 ft long concrete patch. The white spot in the lower frame is spilled slurry. Just below and to the left of the "K" is a 1.5 in. diameter by 10 in. deep bolt hole. Filter: 650 nm.

Figure 5-14. Visible Image of Area M: a 13.5 ft (across trench) by 11.5 ft (parallel to trench) grid. The main feature is a 5.6 ft wide, 2.5-3.5 in. deep trench carved into the asphalt. There is loose gravel and asphalt chunks in the trench. On the far side of the trench is a 1.2 ft wide by 2 in. deep rut. There is hardened slurry in the bottom of a portion of the rut on the right side.

Intensity values, in the form of gray scale counts, were measured for various features in Area G. Results are graphed in Figure 5-15. The gray scale counts were measured by choosing an area in the image containing only the feature of interest and calculating the mean and standard deviation of the pixels inside the area.

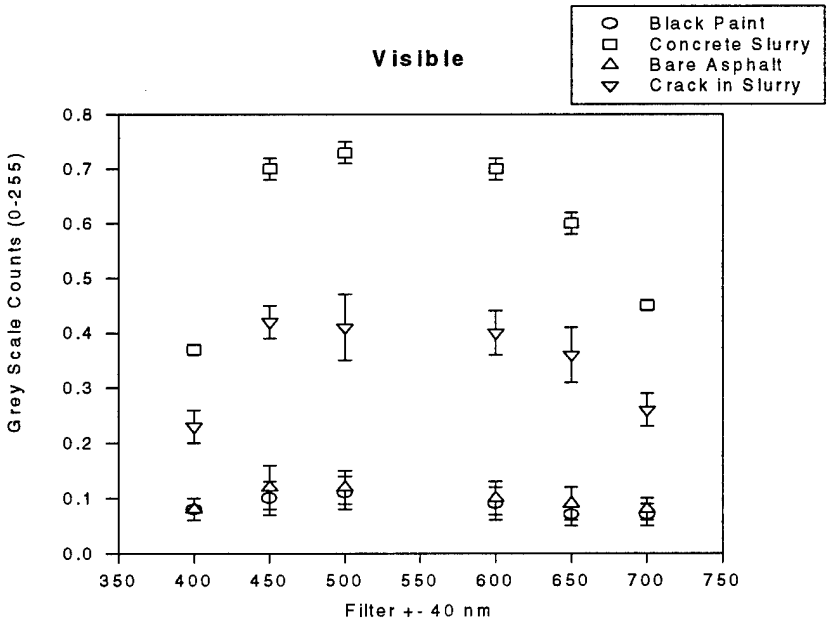

Figure 5-15. Normalized Intensity, Measured in Gray Scale Counts, vs. Frequency for Various Features in Area G

The lighter concrete had higher counts than the darker asphalt and black paint, as expected from the magnitude of the reflection spectra in Figures 3-1 and 3-2. The shape of the curves in Figure 5-15 is a consequence of the spectral response curve of the camera (Figure 5-1) and not a change in reflectivity of the surface as a function of wavelength. Therefore, though the visible images have value, there is no added information to be gained by using a multispectral approach, as predicted in Chapter 3.1.

5.2 THERMAL IMAGES

The thermal images were acquired with an IR scanning radiometer, Inframetrics model 760, which has a minimum detectable temperature difference of ± 0.1°C. The detector in this camera is a mercury/cadmium/telluride with a spectral bandpass of 3-12 μm. There are two filters that can be rotated into the path of the radiation, 3-5 μm and 8-12 μm. The detector response is poor in the 3-5 μm range, therefore data were taken only for the entire 3-12 μm range (no filter) and with the 8-12 μm filter. The height of the camera from the surface of the pavement was 21.25 ft (6.5 m). The viewing angle was approximately 20°, though this varied slightly from one image to another. The average distance between the object plane and the image plane is $L=h/\cos(\theta)=22.6$ ft (6.9 m). The camera must be used with a telescope for proper imaging. We used a 1X telescope and a 3X. The 3X has better resolution but a very narrow field of view. Using the 1X telescope, the instantaneous-field-of-view (IFOV) of the detector is 1.8 mrad. The minimum resolution is $x_{min}=2L\tan(0.0018/2)=0.49$ in. (1.2 cm). There are 194 IFOVs/line, thus the horizontal FOV is 20°. This corresponds to a horizontal FOV of 7.9 ft (2.4 m) at the object plane. The vertical FOV is 15°, which translates to 6.0 ft (1.8 m). For the 3X telescope, the minimum resolution is 0.16 in. (4.0 mm), the horizontal FOV is 2.6 ft (0.8 m), and the vertical FOV is 2.0 ft (0.6 m). It is important to realize that these numbers give the true spatial resolution even though the data is digitized at 256X256 pixels per image.

The most interesting data were taken of Areas A and C, where the voids were excavated beneath 6 in. of asphalt. Since air is a poorer conductor of heat than asphalt, the bulk asphalt cools at a more rapid rate than the air pocket. The air void is hotter than the bulk material and shows up as a light spot in the thermal images. Figures 5-16 through 5-18 are thermal images of Area A taken the night of 11 September. Figures 5-19 through 5-21 are thermal images of Area C also taken the night of 11 September. The cracks and bolt holes show up as well as the subsurface voids. Figures 5-16 through 5-21 were taken with the 1X telescope. Figures 5-22 and 5-23 are some hot spots found in grid J taken with the 3X telescope. These hot spots are unknown subsurface phenomena.

Thermal images of the remaining areas are shown in Figures 5-24 through 5-36. Finally, a grid with various nuts, bolts, sand and aggregate was laid out. Figure 5-37 is the visible image of the grid with the objects labeled. Figure 5-38 is a thermal image of the grid. The objects are clearly visible in the thermal image, showing that it is possible to also distinguish loose debris from bare pavement with this technique.

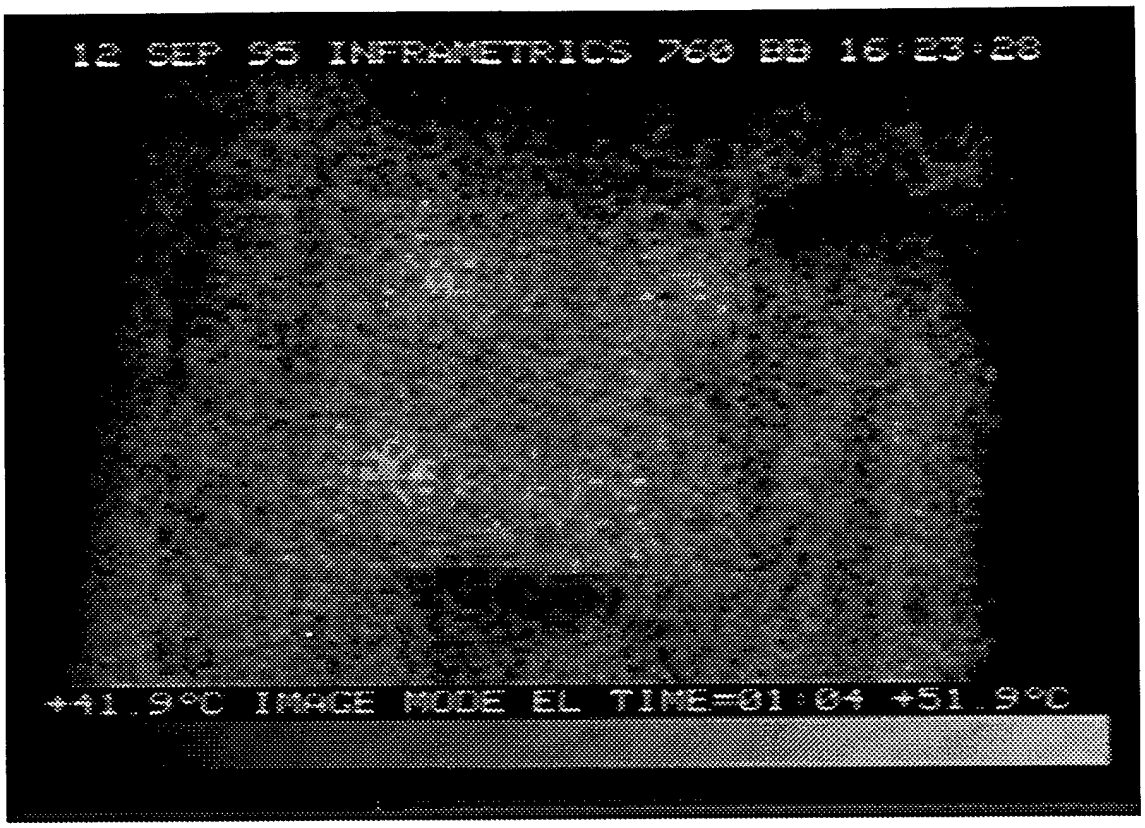

Figure 5-16. Thermal Image of Area A: taken at 1701 hours; ambient temp: 34°C; surface temp: 42.5°C

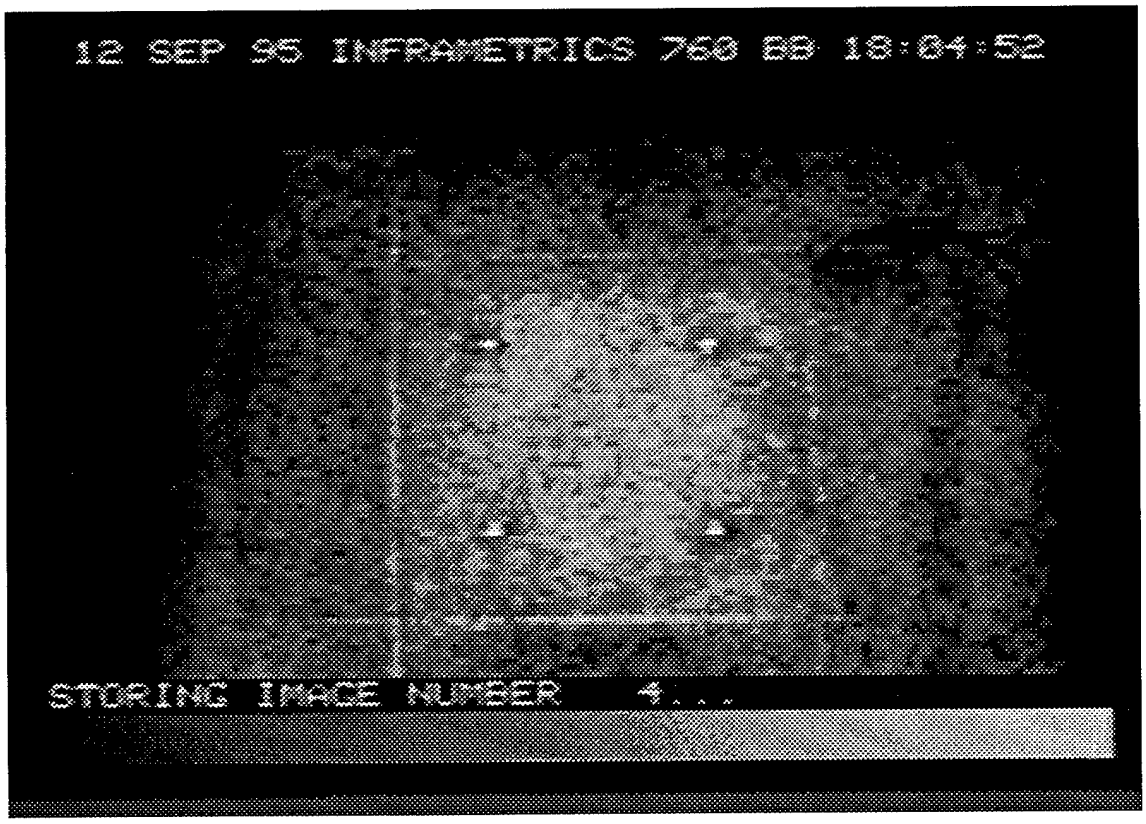

Figure 5-17. Thermal Image of Area A: taken at 1845 hours; ambient temp: 30°C; surface temp: 37.6°C

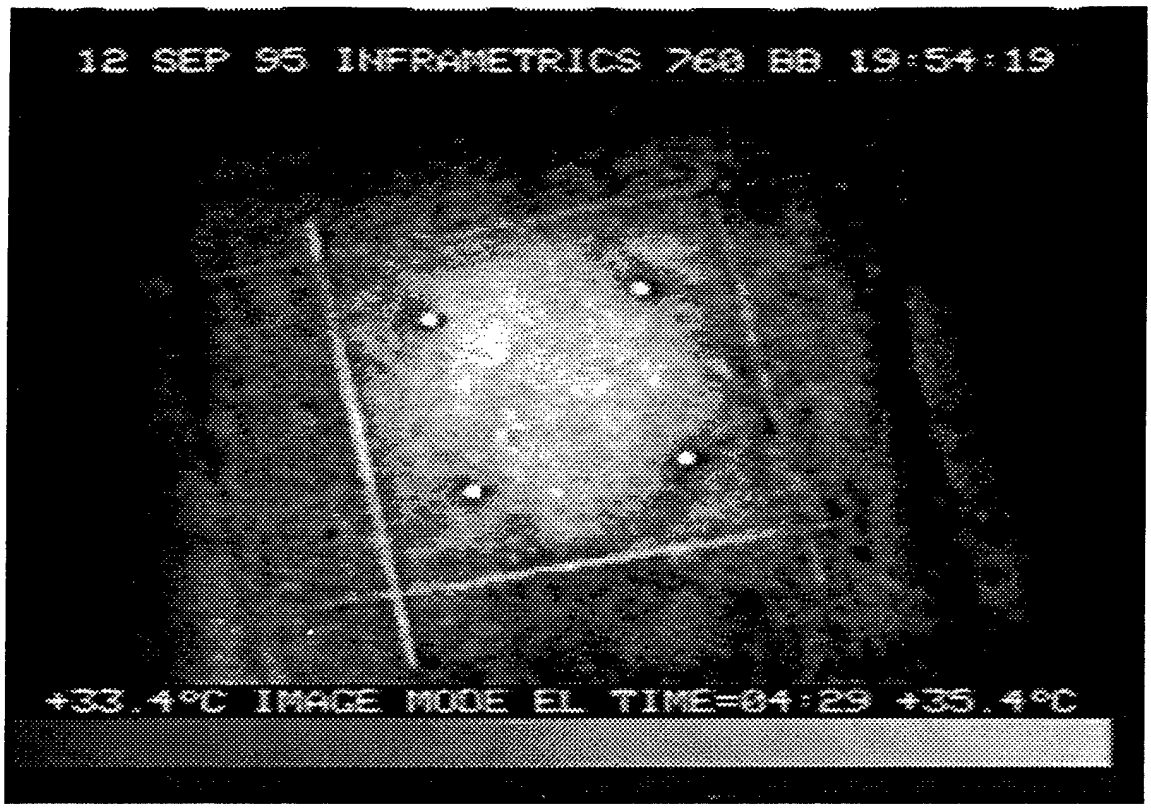

Figure 5-18. Thermal Image of Area A: taken at 2030 hours; ambient temp: 28°C; surface temp: 35.2°C

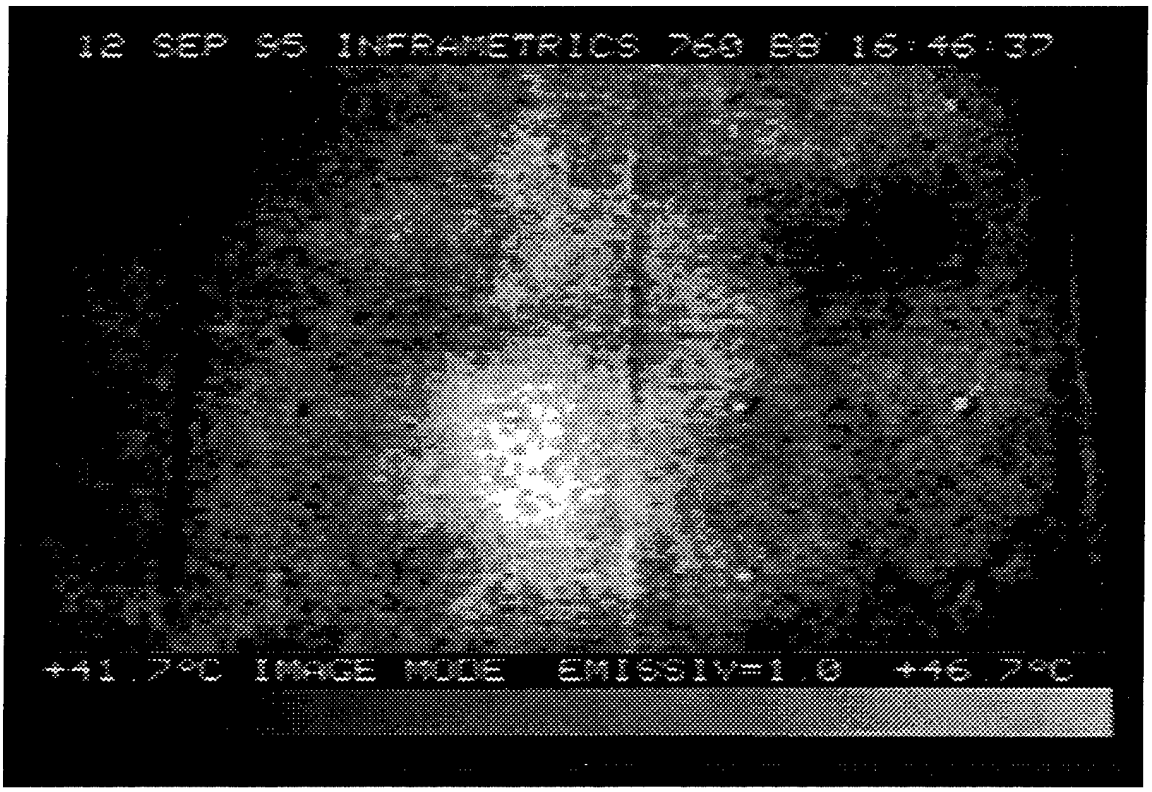

Figure 5-19. Thermal Image of Area C: taken at 1722 hours; ambient temp: 32°C; surface temp: 42.5°C

Figure 5-20. Thermal Image of Area C: taken at 1854 hours; ambient temp: 30°C; surface temp: 37.6°C

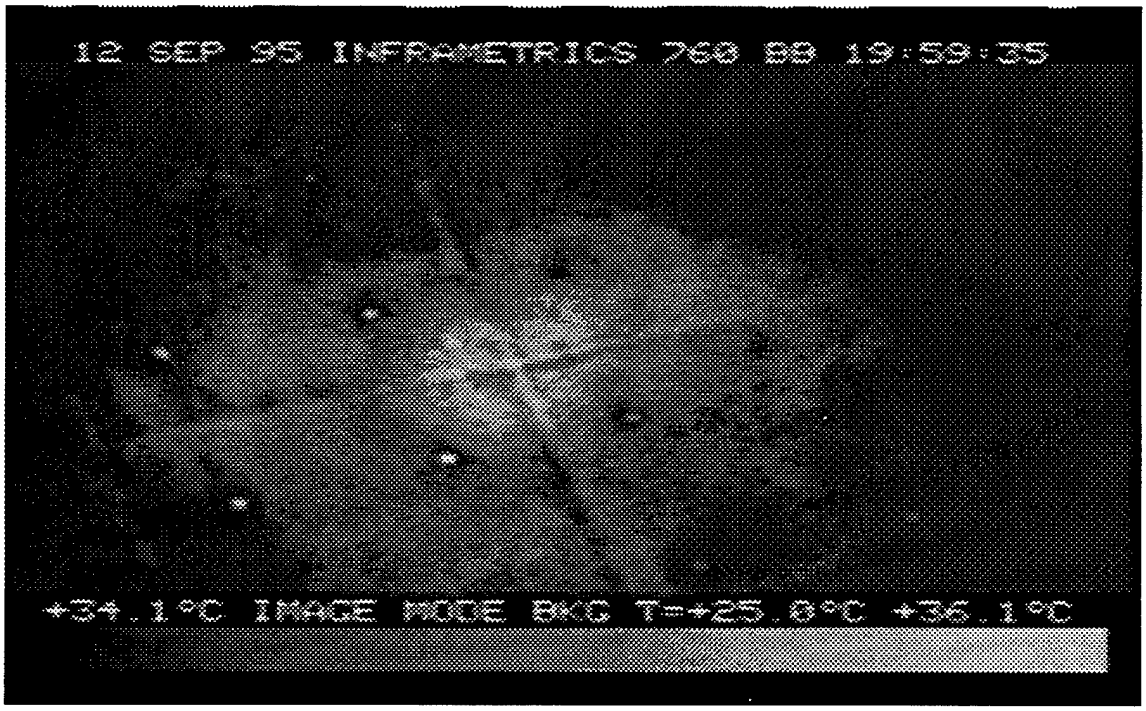

Figure 5-21. Thermal Image of Area C: taken at 2038 hours; ambient temp: 28°C; surface temp: 34.3°C

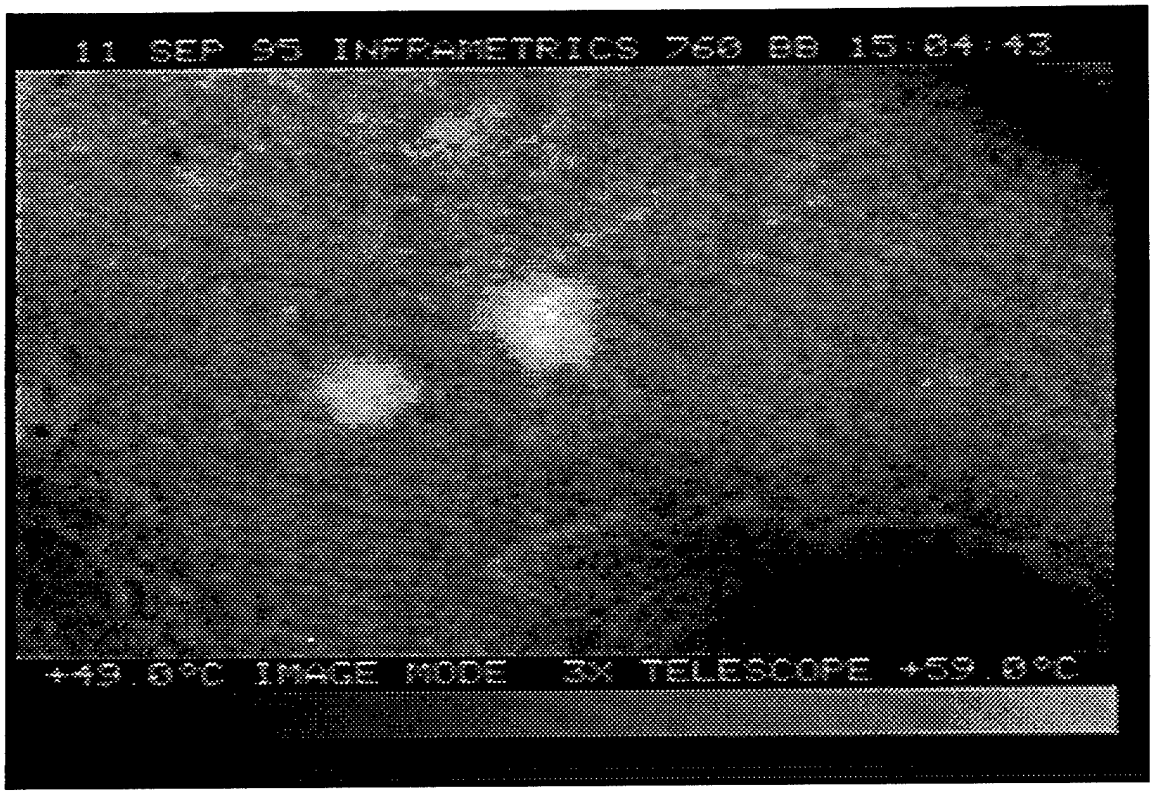

Figure 5-22. Thermal Image of Area J: taken at 1524 hours; ambient temp: 35.5°C; surface temp: 43.0°C

Figure 5-23. Thermal Image of Area J: same as Figure 5-22 but has core hole at far right for reference (image taken facing west)

Figure 5-24. Thermal Image of Area B: taken at 1714 hours; ambient temp: 32.0°C; surface temp: 36.3°C; temp inside hole: 34.7 °C; 1X telescope lens

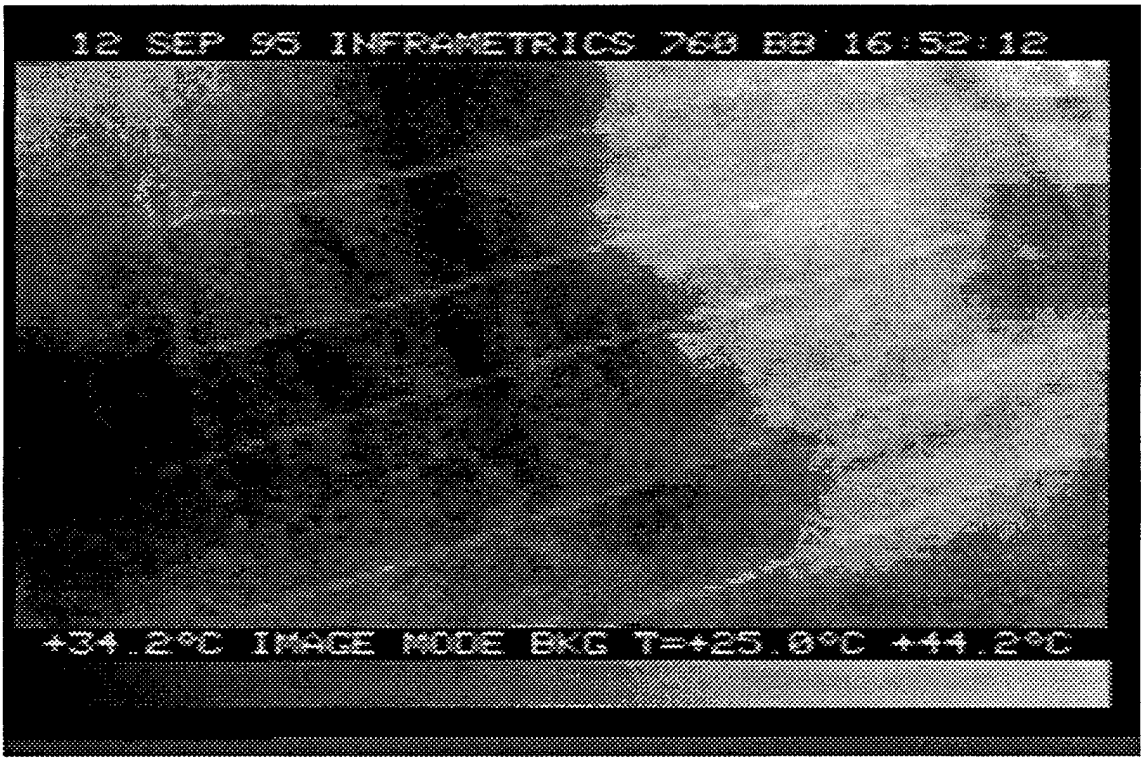

Figure 5-25. Thermal Image of Area D: taken at 1730 hours; ambient temp: 32.0°C; surface temp: 38.9°C; 1X telescope

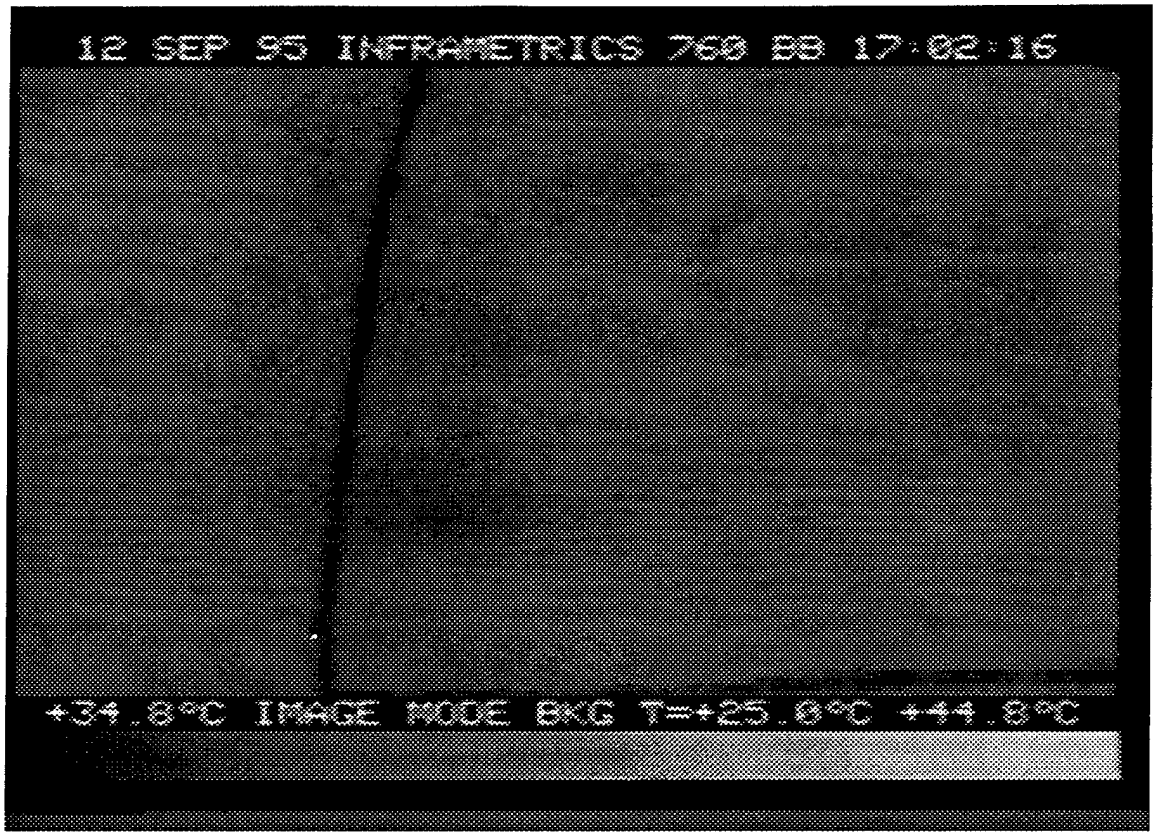

Figure 5-26. Thermal Image of Area E: taken at 1738 hours; ambient temp: 32.6°C; surface temp: 36.3°C; 1X telescope

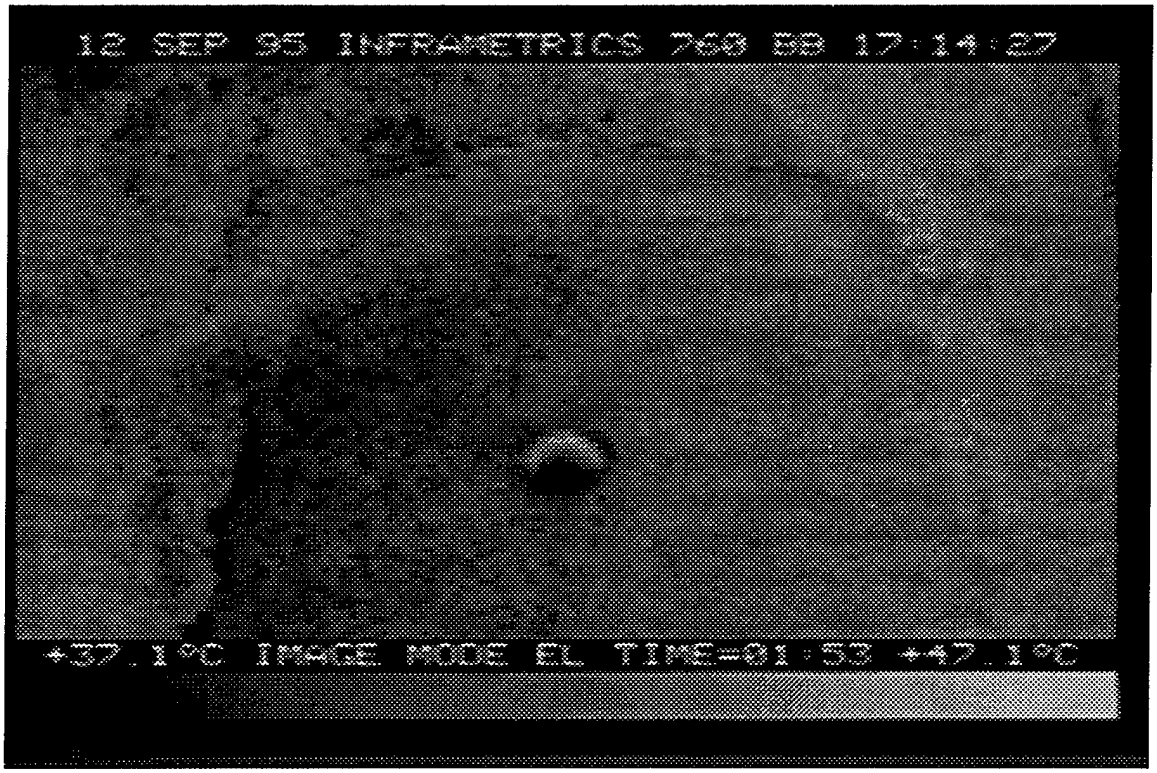

Figure 5-27. Thermal Image of Area F: taken at 1752 hours; ambient temp: 32.6°C; surface temp: 38.3°C; temp inside hole: 36.0 °C; 1X telescope

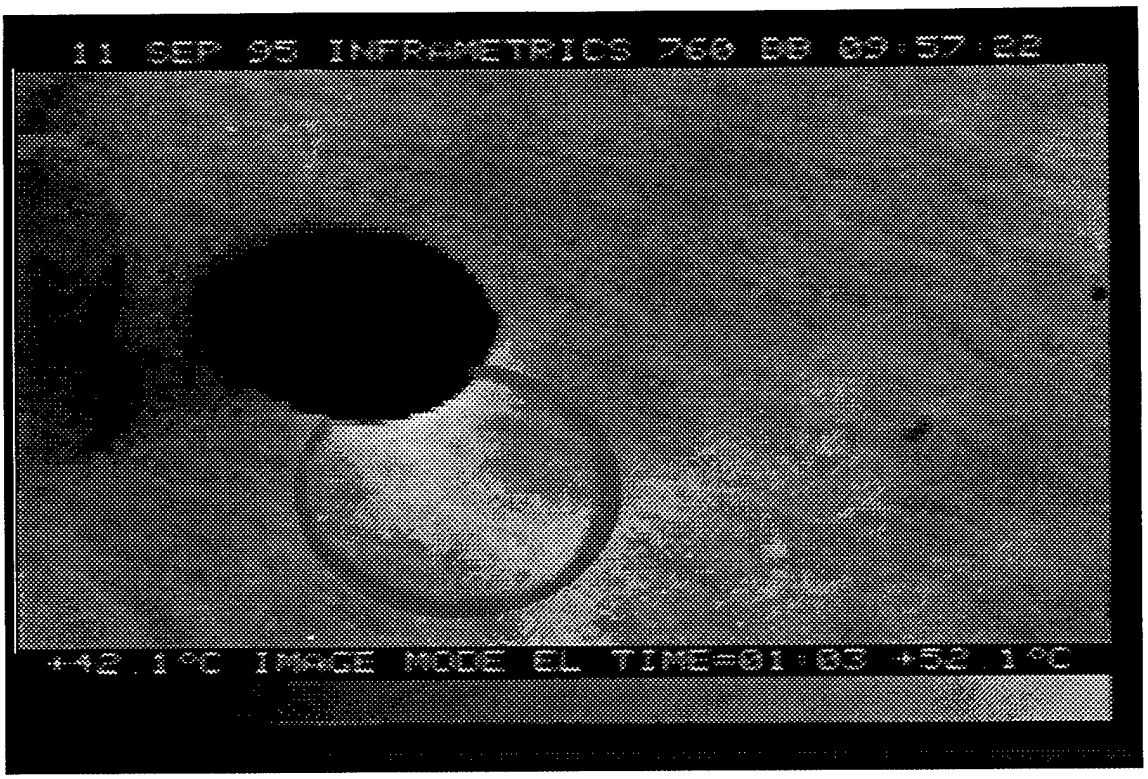

Figure 5-28. Thermal Image of Area F: taken at 1032 hours; ambient temp: 34.0°C; surface temp: 40.5°C; temp inside hole: 36.4 °C; 3X telescope. There was standing water in the hole. The circled area shows a hot spot indicating a region of delamination.

Figure 5-29. Thermal Image of Upper Portion of Area G: taken at 1756 hours; ambient temp: 32.0°C; surface temp: 37.0°C; 1X telescope

Figure 5-30. Thermal Image of Area H: taken at 1928 hours; ambient temp: 29.0°C; surface temp: 33.6°C; temp of hole crack: 34.5 °C; 1X telescope

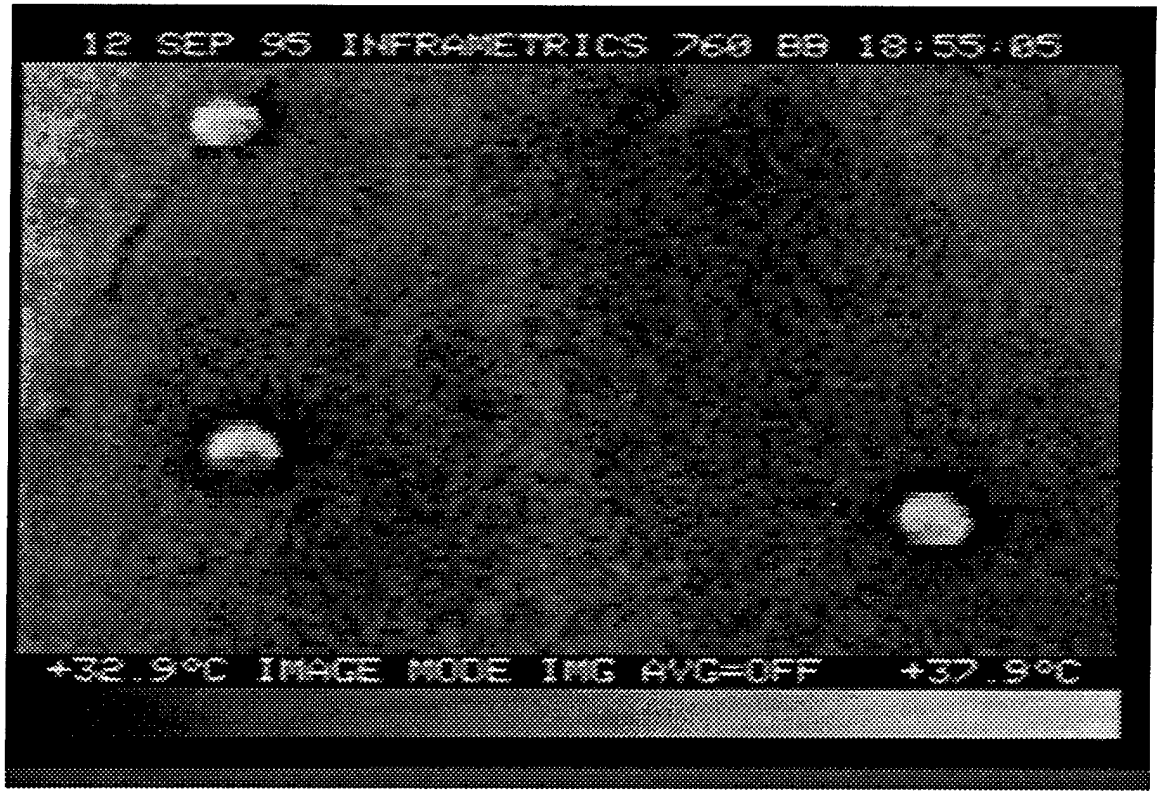

Figure 5-31. Thermal Image of Area I: taken at 1931 hours; ambient temp: 29.0°C; surface temp: 33.6°C; temp inside hole (lower right): 33.9 °C; 1X telescope. Standing water in lower left hole.

Figure 5-32. Thermal Image of Area J: taken at 1937 hours; ambient temp: 29.0°C; surface temp: 33.3°C; dark spot around hole is water; 1X telescope

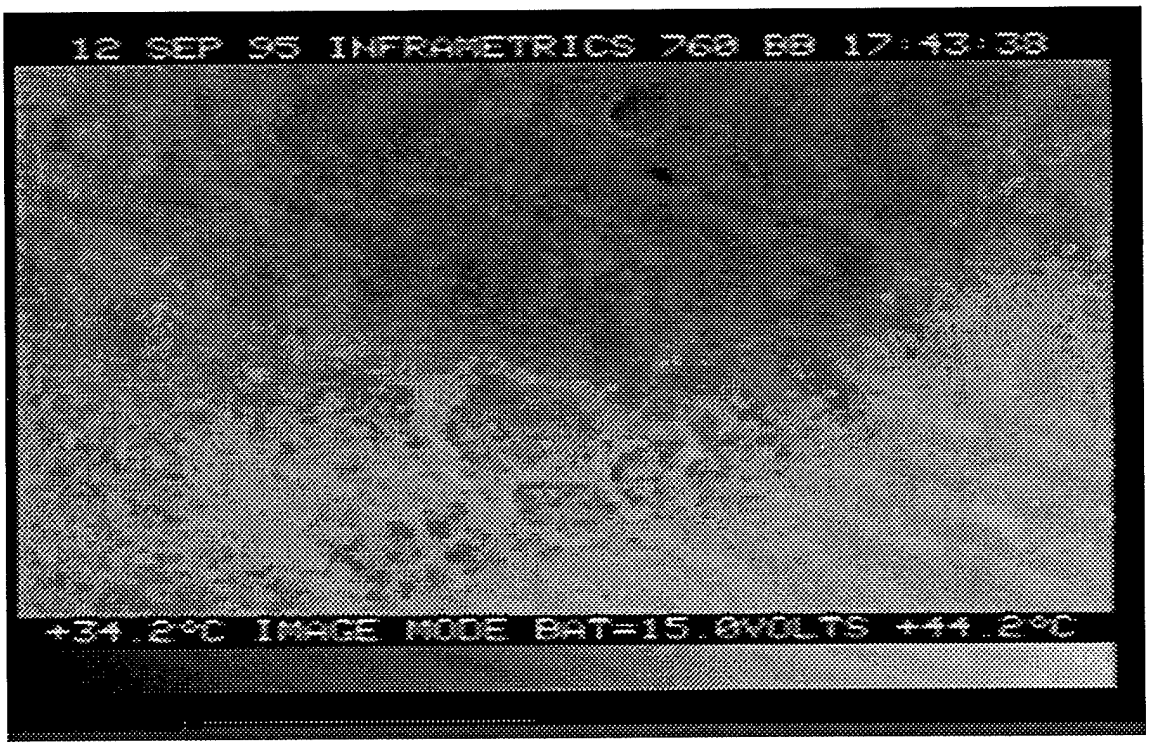

Figure 5-33. Thermal Image of Area K: taken at 1820 hours; ambient temp: 30.5°C; surface temp: 35.2°C; 1X telescope. Just below patch is an old, worn paint stripe.

Figure 5-34. Thermal Image of Area L: taken at 1826 hours; ambient temp: 30.0°C; surface temp: 35.7°C; 1X telescope. The rut runs vertically through middle of image. There is a weed growing in the middle of the trench. Just to the right of that is a 4 in. diameter core hole. The two bright spots are 1.5 in. diameter bolt holes.

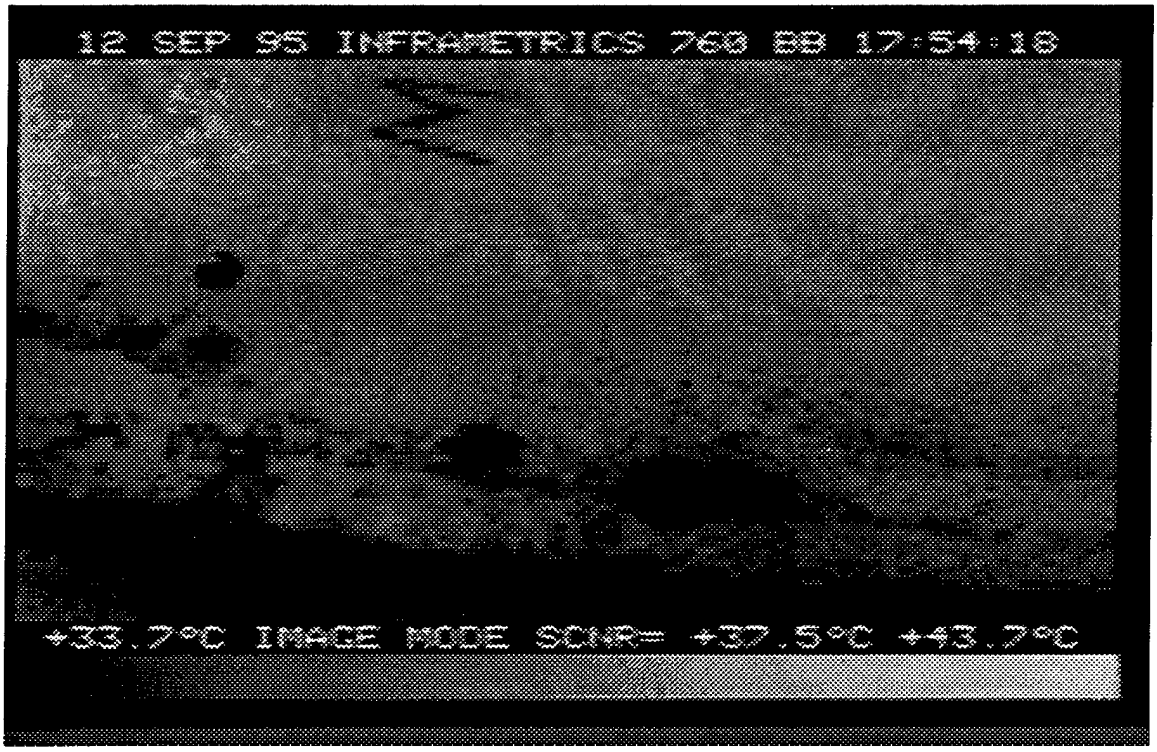

Figure 5-35. Thermal Image of Upper Left Corner of Area M: taken at1832 hours; ambient temp: 30.0°C; surface temp: 35.5°C; 1X telescope. The rut runs horizontally across the image. The trench is visible at the bottom of the image.

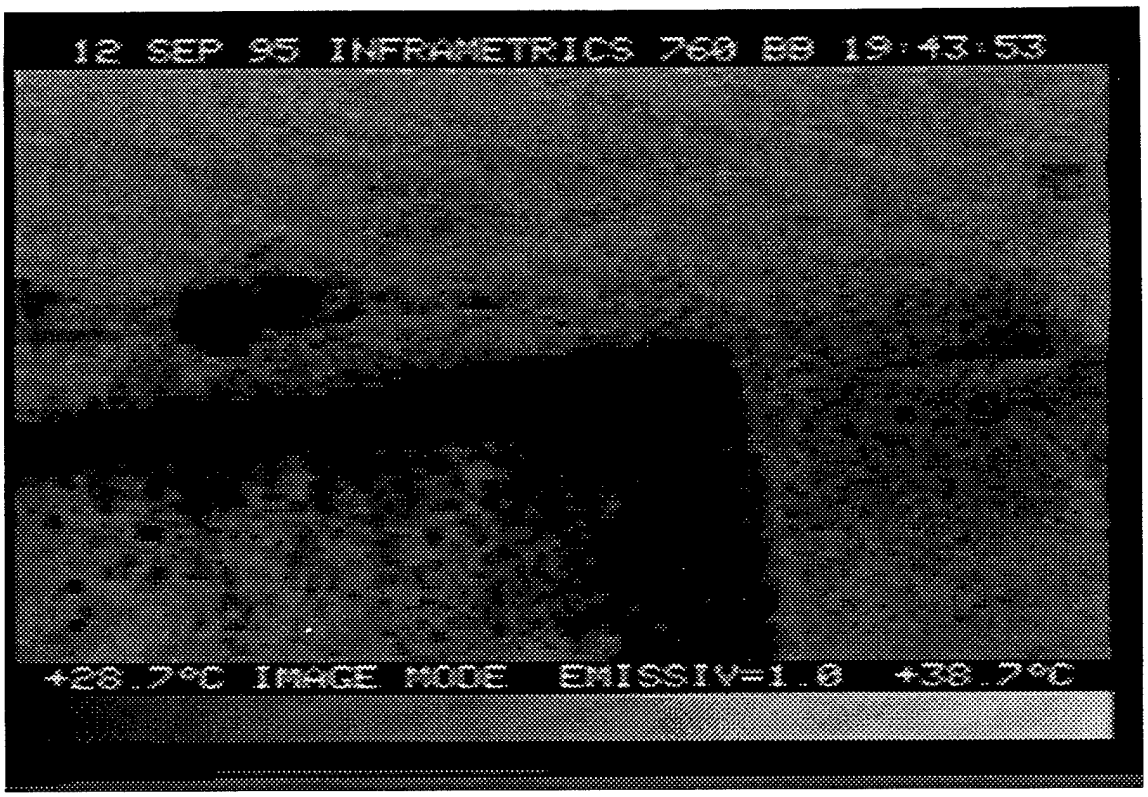

Figure 5-36. Thermal Image of Lower Left Corner of Area M: taken at 2019 hours; ambient temp: 28.5°C; surface temp: 33.1°C; 1X telescope. Loose asphalt is visible in the corner of the trench.

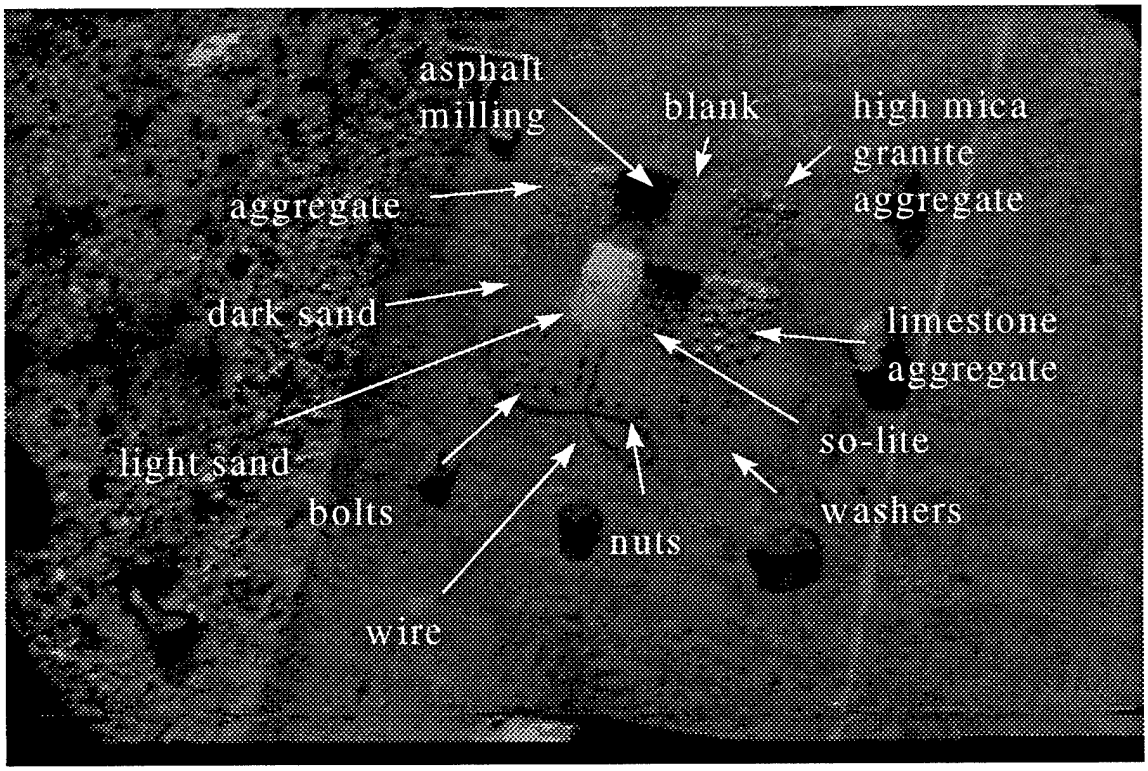

Figure 5-37. Visible Image of Grid with Various Small Objects

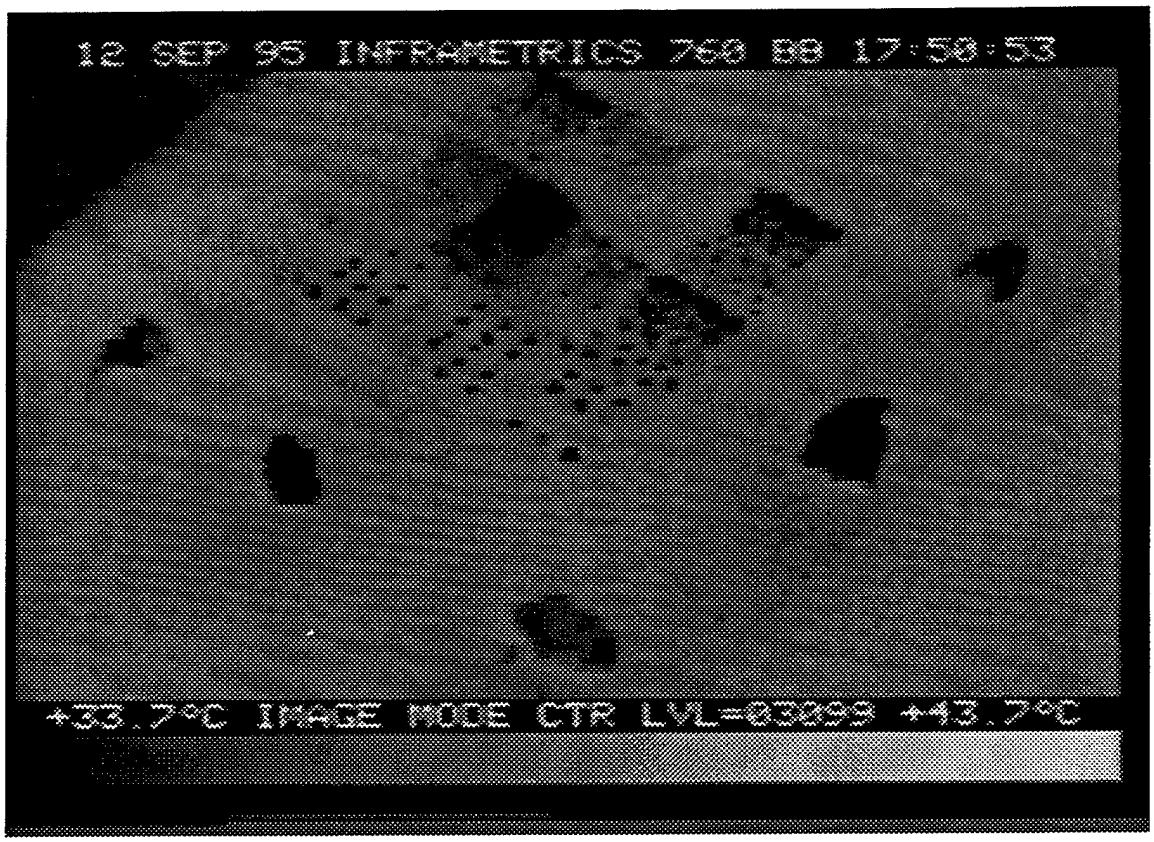

Figure 5-38. Thermal Image of Grid in Figure 5-37: taken at 1826 hours; ambient temp: 30.0 °C. The edge of the pavement is clearly visible along with the narrow paint stripe.

The thermal images clearly show both surface and subsurface effects. The surface effects show up more clearly in the early morning during periods of heating. The subsurface voids show more clearly in the late evening during periods of cooling. Contrast ratios were calculated for the voids in Areas A and C, and for the cracks in Areas D and E. The contrast ratio is defined as

$$C = \frac{I_{max} - I_{min}}{I_{max} + I_{min}}, \qquad (5\text{-}1)$$

where I_{max} and I_{min} are the maximum and minimum pixel gray scale values. An area was chosen containing only pixels illuminated by the crack or void and the mean and standard deviation of the gray scale value (0-255) of those pixels was calculated. The mean was assigned to I_{max}. A second area was chosen on the background near the crack or void and the process was repeated. The mean value of the background was assigned to I_{min}. The contrast was then calculated using Equation (5-1). This process was repeated for several frames of the same image taken at the same time. The contrast ratio for the voids is plotted versus the time of day in Figure 5-39. The negative values for the contrast ratios mean that the void (or crack) was cooler than the background and was therefore darker (less counts) in the image. The contrast ratios for the cracks in Areas D and E versus time of day are plotted in Figures 5-40 and 5-41. At 1000 hours, the cracks in the concrete slurry of Area E were cooler than the bulk material resulting in a negative contrast ratio. Figure 5-42 is the contrast ratio versus time of day for Area E with the vertical axis adjusted to suppress the negative contrast values. This was done for easier

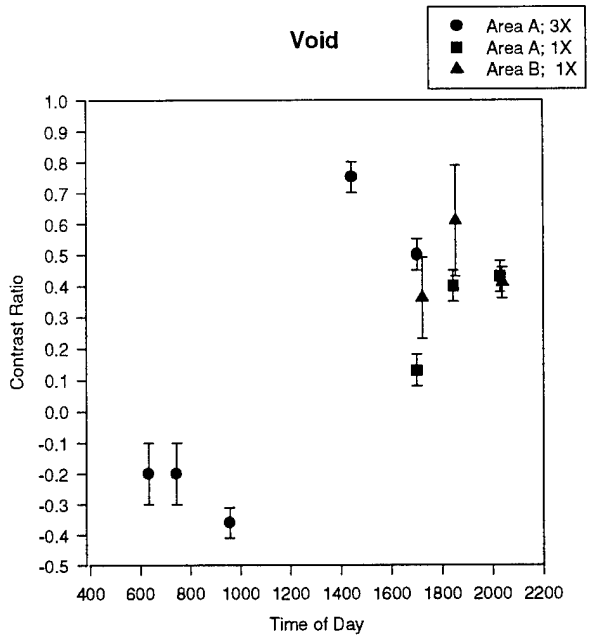

Figure 5-39. Contrast Ratio vs. Time of Day for Voids in Areas A and C

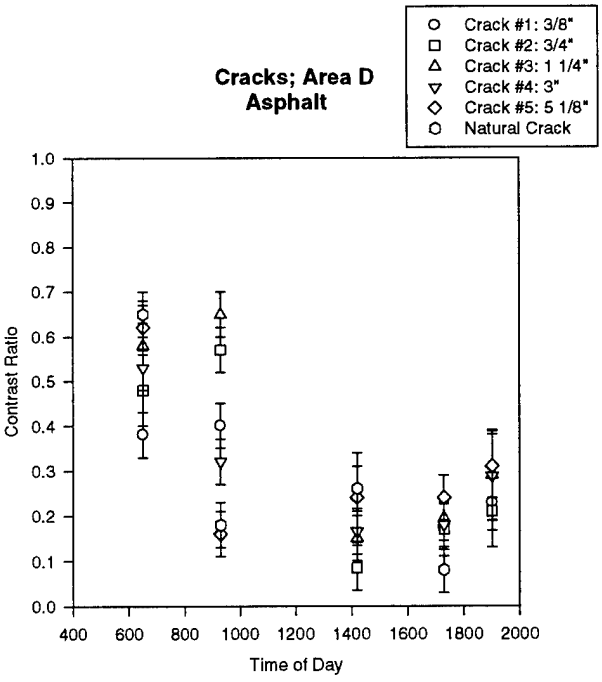

Figure 5-40. Contrast Ratio vs. Time of Day for Cracks in Area D

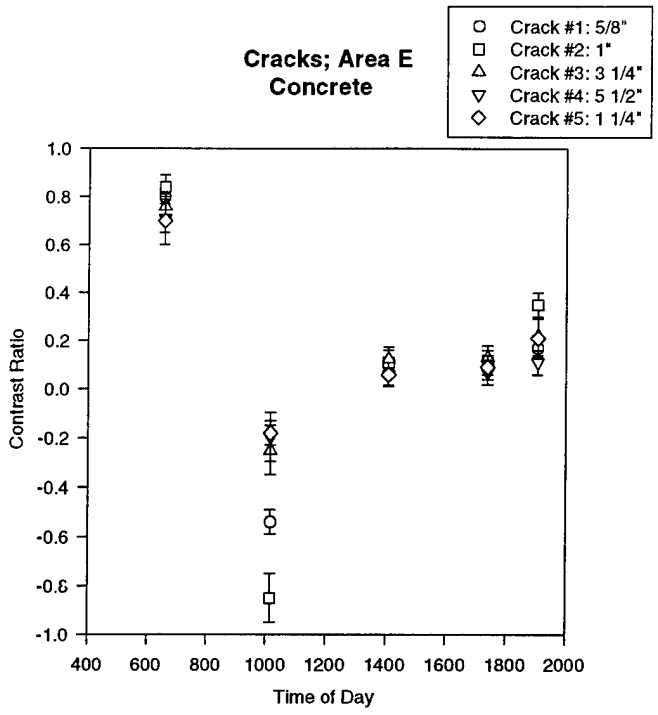

Figure 5-41. Contrast Ratio vs. Time of Day for Cracks in Area E

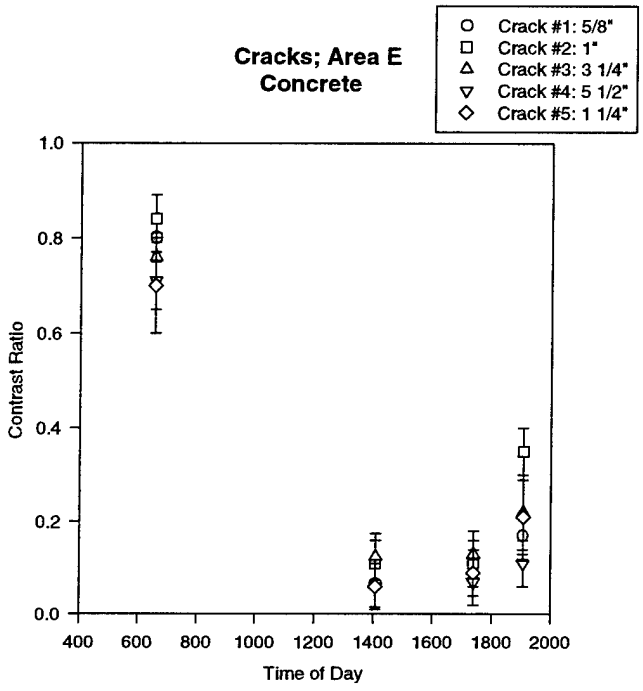

Figure 5-42. Contrast Ratio vs. Time of Day for Cracks in Area E with Negative Values Suppressed

comparison to Figure 5-40, the cracks in Area D. The statistical error was first calculated from the standard deviations of the pixel counts, but it was found to be much smaller than the standard deviation of the frame-to-frame contrast ratios. The frame-to-frame standard deviation was therefore used as error bars in the plots.

The cracks were cut into the pavement at varying depths. They are numbered from one to five starting with the first crack at the bottom of the frames in Figures 5-25 and 5-26. The depth of each crack is shown in the legend on each plot for Areas D and E.

Temperature measurements were taken at the surface and inside each crack during each measurement. Plots of contrast ratios versus temperature are shown in Figures 5-43 through 5-46 for the voids and the cracks in Areas D and E.

The voids are cooler than the bulk material in the early morning during periods of heating and the contrast is poor. The contrast ratios measured in the evening are lower than they should be because Areas A and C were painted black that morning. The black paint absorbed and retained the heat more than the bare pavement, resulting in a higher background count. The plot in Figure 5-43 of contrast ratio versus temperature shows that the voids are more visible when the temperature is maximum. This may be misleading, since the maximum temperature measurement corresponds to that taken at 1400 hours. This measurement was taken on the day before the areas were painted black. Painting these areas has, unfortunately, skewed this data.

The contrast ratios for the cracks are greatest in the early morning during periods of heating. This was also true for all the surface phenomena. There is a crossover point about midmorning when the temperature of the bulk material exceeds the temperature of the surface anomaly. When this crossover occurs will depend on the thermal properties of the material; the thermal conductivity and the specific heat. While these quantities are independent of each other, they both contribute to the apparent temperature of the surface as measured by the thermal camera. The thermal conductivity is a measure of the rate that energy is transferred through the bulk material. If the conductivity is high, the energy will be rapidly distributed throughout the bulk of the material. The surface temperature will appear to be less than that of a material with lower conductivity because, for the lower conductivity material, the heat energy will remain at the surface longer. From the CRC Handbook, the thermal conductivity of asphalt is 0.06 W/(m K) and concrete is 0.8 W/(m K).[8] The specific heat is the amount of energy required to raise the temperature of the material. If the specific heat is low, less energy is required to raise the temperature. The surface will be hotter than a material with higher specific heat exposed to the same energy (i.e., the sun). The specific heat of concrete is 0.23 cal/(gm °C), while the specific heat of asphalt is 0.40 cal/(gm °C). It takes about half as much energy to raise the temperature of concrete as it does for asphalt. These are the reasons why the contrast ratio for the cracks in the concrete of Area E are negative (the temperature of the bulk is hotter than the cracks) at 1000 hours whereas the cracks in the asphalt of Area D are still hotter than the bulk at 1000 hours.

During the hottest part of the day the cracks are least visible, as seen from the plots in Figures 5-44 through 5-46. There is another crossover point when the surface begins to cool and the cracks appear hotter than the bulk material. This is because the heat energy is radiated from the hotter subsurface through the cracks. Unfortunately, there is little data for these crossover points.

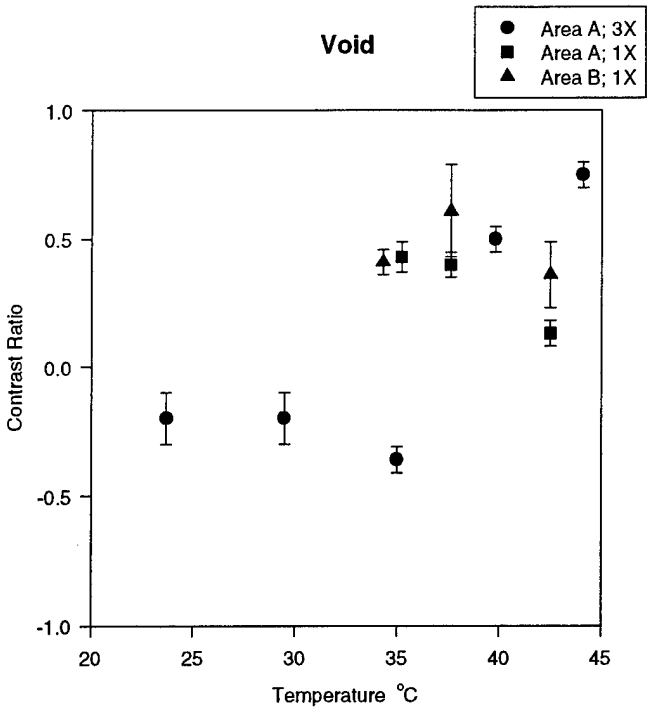

Figure 5-43. Contrast Ratio vs. Temperature for Voids in Areas A and C

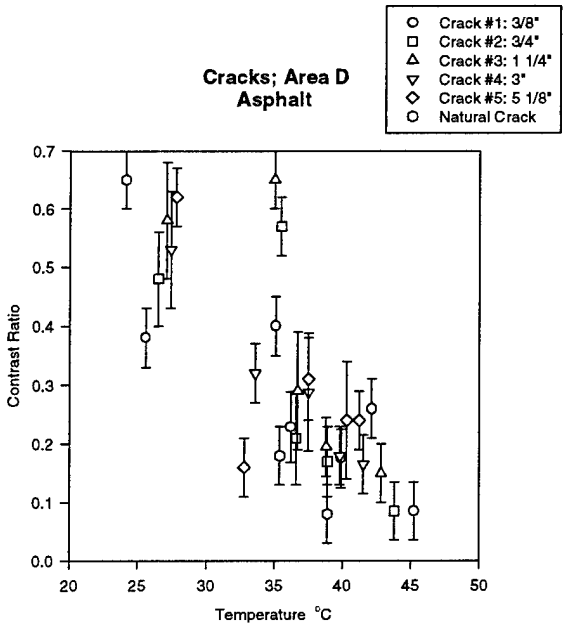

Figure 5-44. Contrast Ratio vs. Temperature for Cracks in Area D

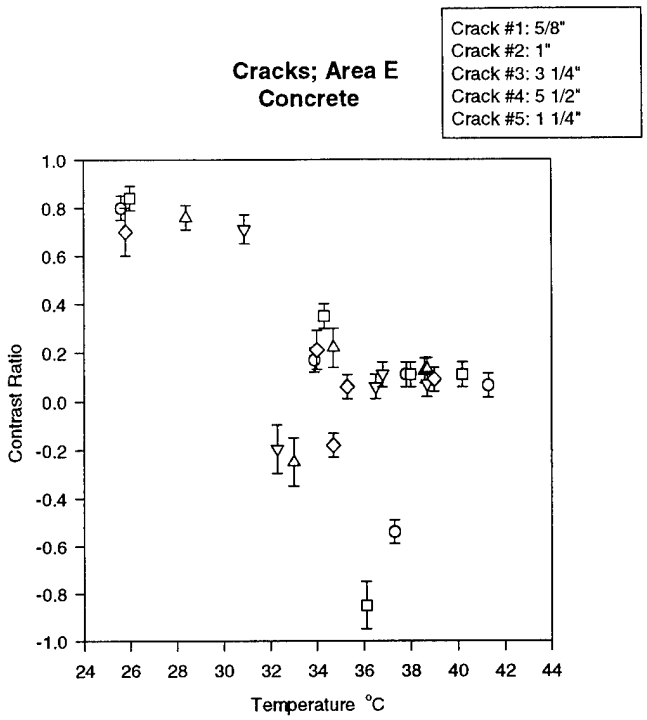

Figure 5-45. Contrast Ratio vs. Temperature for Cracks in Area E

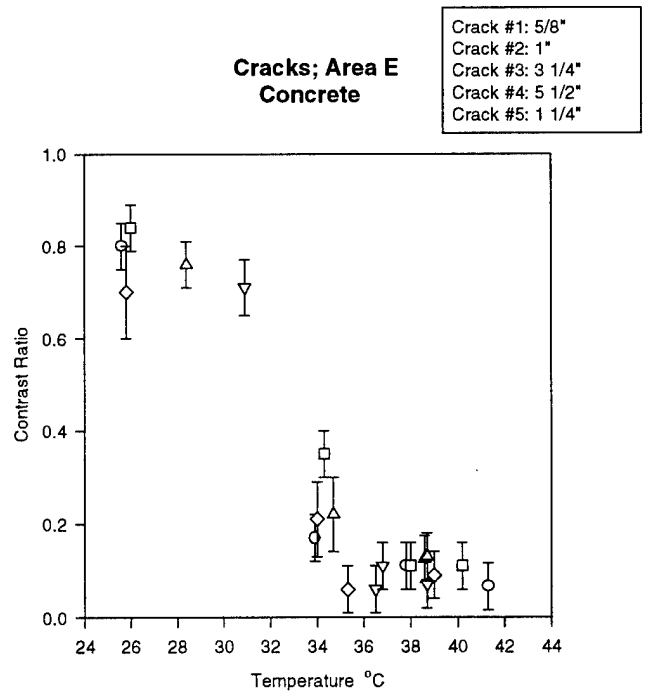

Figure 5-46. Contrast Ratio vs. Temperature for Cracks in Area E with Negative Values Suppressed

CHAPTER 6

IMAGE PROCESSING

Image processing provides a large range of techniques which can be useful in automating the analysis of imagery to determine the amount of damage to a runway. Several techniques are described and applied to the field test imagery. This study demonstrates the viability of some of these techniques, and is not meant to be either exhaustive or a complete solution to the problem.

6.1 MATHEMATICAL MORPHOLOGY

Grayscale morphology techniques can be very useful in cases where one wishes to identify pixel clusters that are dark compared to a surrounding relatively light background or pixel clusters that are light compared to a surrounding relatively dark background. In particular, the "top-hat" transformation (white or black) combined with other basic morphological operations can be shown to be very useful in these types of situations.[9] The white top-hat transformation is defined as the absolute difference between the image and the "opened" image, where the "opening" is a basic morphological operation which is geometry based and requires the use of an appropriate "structuring element." Correspondingly, the black top-hat transformation is defined as the absolute difference between the image and the "closed" image. Again, an appropriate geometric structuring element is required.

Conceptually, if we view the grayscale image signal as a 2-dimensional relief then the top-hat transformation will extract the peaks or valleys that jut above or below the local surrounding terrain.[10] In particular, peaks (valleys) whose bases (mouths) are narrower than the width of the flat 2-dimensional structuring element will be highlighted. For example, disks, lines, and polygons are commonly employed as structuring elements in the operations. The idea is that by changing the size and shape of the structuring element we may control which objects are extracted from the image, based on their size and shape. The figures below show an example of the application of these techniques.

In this example, the original image shown in Figure 6.1 was opened using a disk of diameter 15 pixels and the result was subtracted from the original. The top-hat transformed image is also shown in Figure 6-1. Now, the image need only be thresholded to extract the desired signal peaks (bottom image in Figure 6-1).

In more complicated situations, further processing following the thresholding step may be needed to eliminate groups of pixels that are not the desired size and shape. Further, if we are

looking for pixel clusters of different sizes we may need to perform these operations several times with different sized and shaped structuring elements and then add the results together. This can best be understood as a "sieving process," i.e., if an image is considered as a collection of grains, then whether or not an individual grain will pass through the sieve depends on its size and shape relative to the mesh of the sieve.[11] A more difficult example is shown below where extended processing was required. The original image is shown in Figure 6-2 and the extracted areas of interest are shown below. It can be readily understood that the false detections that are difficult to eliminate are those that are the same size, shape, and relative brightness as the patches we are seeking. In Figure 6-2 the false detections are marked with circles.

It may also prove advantageous in these problems to employ a "high-boost filter." This filter seeks out small clusters of pixels that are slightly brighter than the immediate background. It has been successfully employed in astronomical applications and has recently been utilized to identify microcalcifications in mammograms.[12] The results gained from using the high-boost filter are similar to those presented here although at a slightly higher computational cost. One advantage of using this filter however is that the need for a geometric structuring element is eliminated.

It should be mentioned that although these morphological techniques are very powerful, they do need to be customized somewhat for each individual class of images and objects of interest. One potential solution to this problem would be to employ an *adaptive* white (or black) top-hat operator.[13] These operators address the problems that can occur when one attempts to choose a single structuring element size in cases where the objects of interest have multiple or unknown widths. Such adaptive methods warrant further study given the variable nature of the runway corruption.

Although we have discussed difficult cases so far, where the difference in contrast between target and background is slight, it should be noted that even simpler techniques may be applied in cases where there is significant contrast.

As is shown in Figure 6-3, we may easily extract the light regions by thresholding the image at an appropriate gray level. The example bellow required using two different thresholds and adding the results together after performing some simple morphological operations.

Thus, the primary conclusion of this portion of the study is the following: algorithms currently exist that are capable of extracting interesting regions from an image that have some degree of contrast with the local background. These techniques vary both in complexity and in their ability to be implemented in a general and automated context. Further investigation using a large ground-truthed database would be needed in order to develop a useful and fully automated procedure.

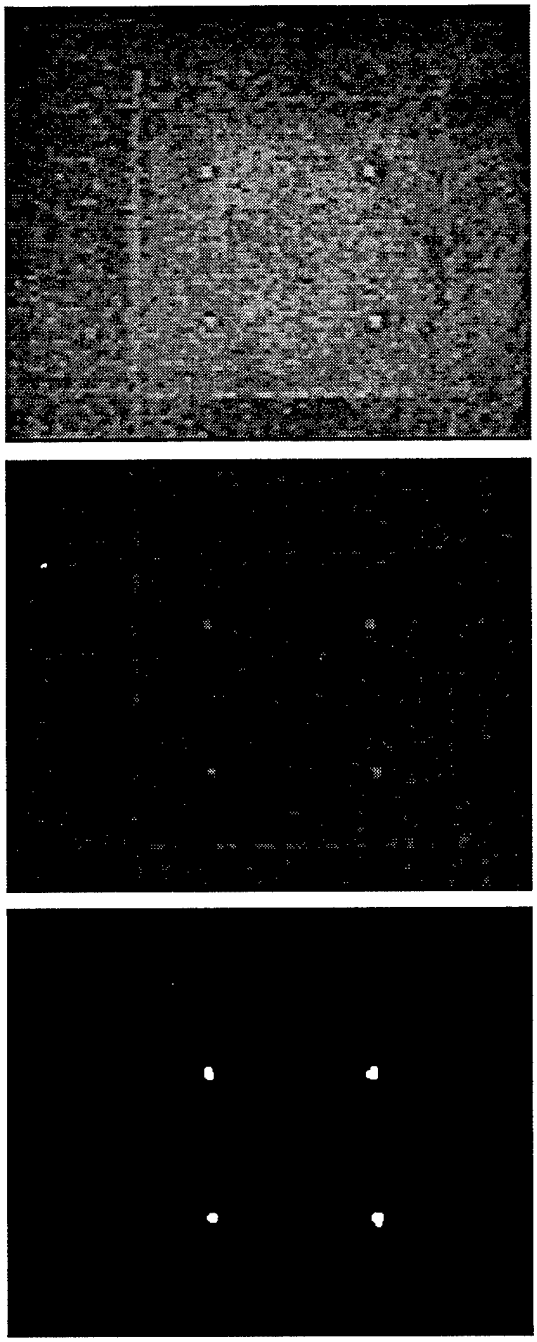

Figure 6-1. Original (Thermal) Image of Area A taken at 1845, Top-Hat Transformed Image, and Thresholded Top-Hat Transformed Image

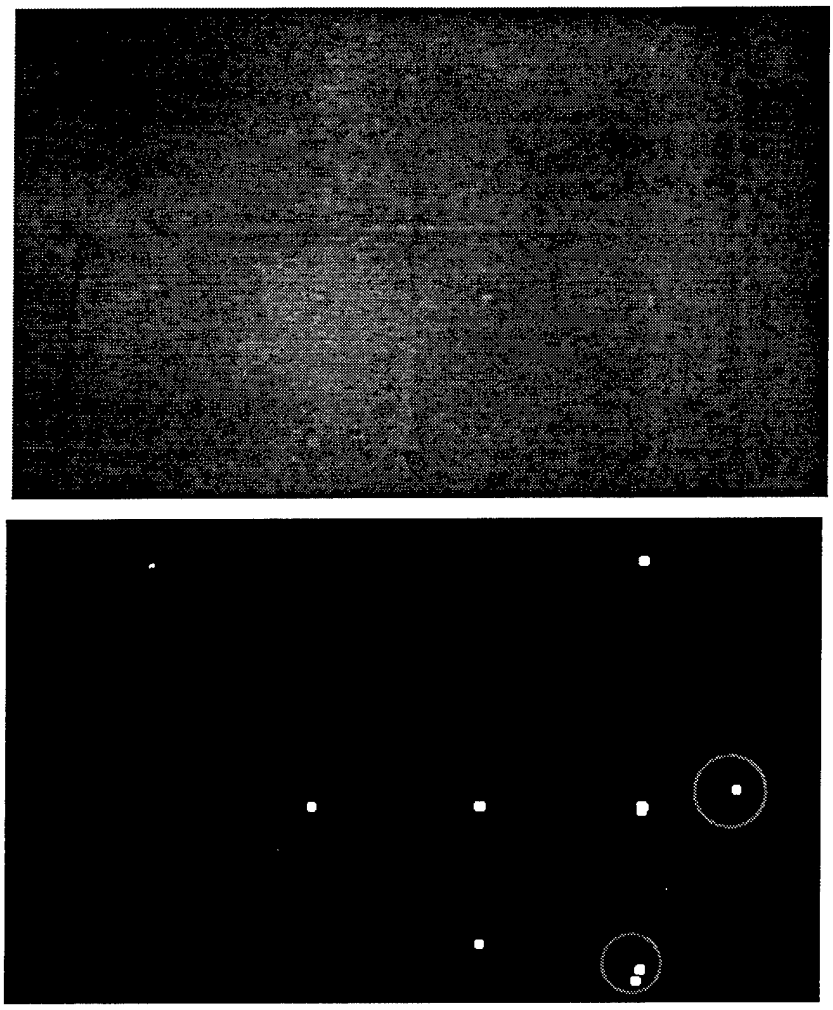

Figure 6-2. Original (Thermal) Image of Area C Taken at 1722 with Extracted Areas of Interest. False alarms are circled.

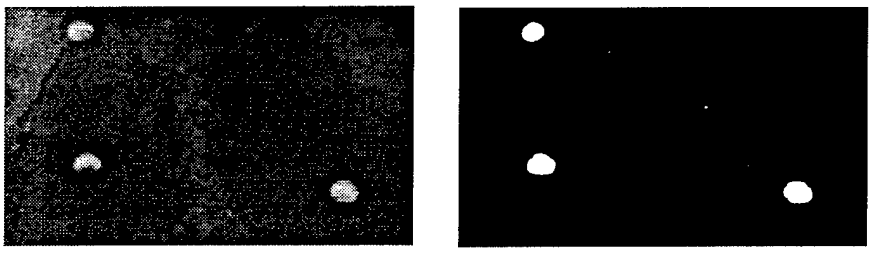

Figure 6-3. Original (Thermal) Image From Area I Taken at 1931 with Holes Extracted Through Thresholding

6.2 MAP SMOOTHING

Intensity differences can be used to detect hidden voids in thermal images, as discussed above. It can be useful to smooth these images to better determine the extent of the void. One method for performing this smoothing is via *Maximum A Posteriori* (MAP) estimation.[14] In the implementation described here, the MAP estimator utilizes a mixture model which has been fit to the intensity values. The intensity values were modeled as a mixture of two components, a low intensity and high intensity component. Once a model is fit, the MAP precedes as follows:
Let

$$p_x^1(v) = p_x(v) = \frac{\pi_x f_x(x)}{\sum_{x \in \{low, high\}} \pi_x f_x(v)} \tag{6-1}$$

where

$$f(v) = \sum_{x \in \{low, high\}} \pi_x f_x(v) \tag{6-2}$$

is the mixture model at the pixel v. The method proceeds by replacing the posterior probability of each pixel with that obtained by considering its neighbors as indicated below. For this example, the neighbors consisted of a 3x3 neighborhood around the pixel. This is iterated until convergence.

$$p_x^{iter}(v) = \frac{\prod_{w \in N(v)} p_x^{iter-1}(w)}{\sum_{y \in \{low, high\}} \prod_{w \in N(v)} p_y^{iter-1}(w)}, \tag{6-3}$$

$$M^{iter}(v) = \begin{cases} 0 & max\left(p_x^{iter}(v)\right) = p_{low}^{iter}(v) \\ 1 & max\left(p_x^{iter}(v)\right) = p_{high}^{iter}(v), \end{cases} \tag{6-4}$$

$$M^{fc}(v) = M^{maxiter}(v). \tag{6-5}$$

The new image M is a mask with nonzero values indicating regions of greater than normal intensity. An example is shown in Figure 6-4.

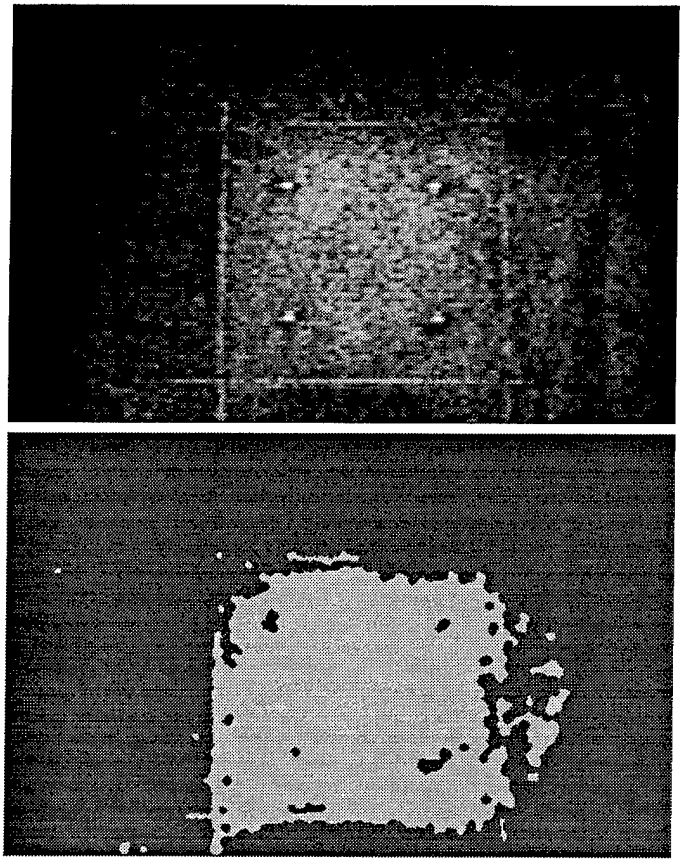

Figure 6-4. Original (Thermal) Image of Area A Taken at 1845 and MAP Region

6.3 HOUGH TRANSFORM

One way to characterize certain types of damage to runways is as geometric objects. Troughs and gouges tend to be long and thin, with roughly parallel delimitating lines. Thus it could be useful to detect lines within an image, for further processing to determine whether the lines are indicative of damage or not. Note that lines can occur from many benign processes as well: tire tracks and painted lines in the visible spectrum, the edges of the runway and the edges of segments of the runways in both visible and thermal images can show up as lines. Thus further processing is required to determine whether the structures indicate damage to the runway.

Edge detection is a well researched area within image processing,[15] and many techniques have been proposed. Most work fairly well for images with little noise and fairly well defined edges. However, the thermal images have a considerable amount of noise, and the edge maps generated tend to be very difficult to interpret (see Figure 6-5, which shows a Sobel edge map[15]). Further, the edges are not grouped into line segments, and it is not clear how best to accomplish this grouping.

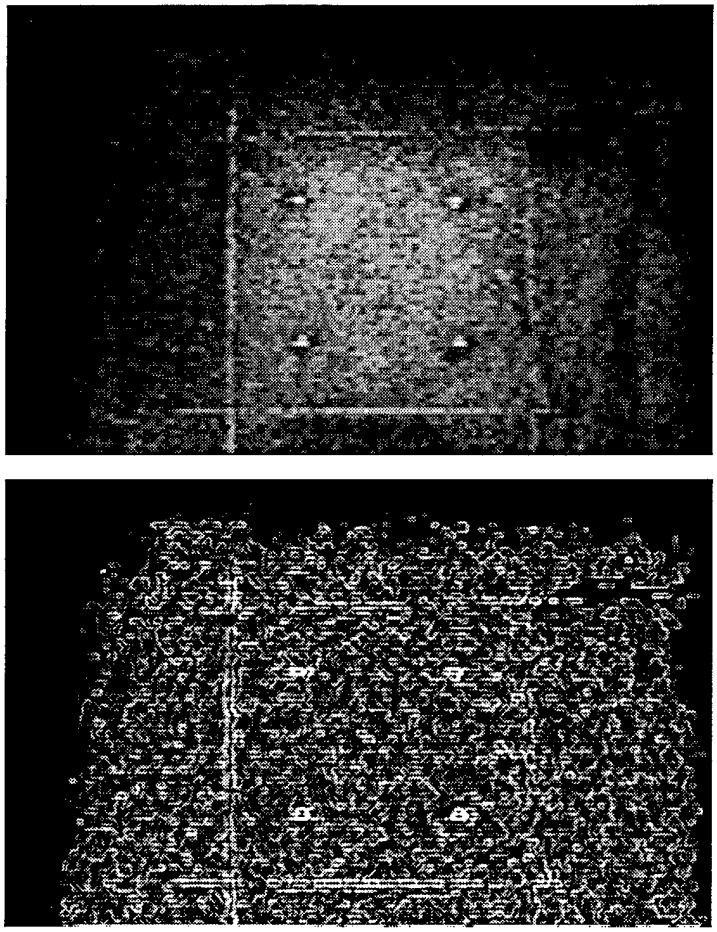

Figure 6-5. Original (Thermal) Image of Area A Taken at 1845 and Sobel Transform

The Hough transform[15] was designed to accomplish the grouping of edges into lines. In the simplest implementation, the Hough transform operates on an edge map, obtained by thresholding an edge extraction algorithm such as the Sobel transform. The transform works by finding neighboring pixels which lie on a line, and keeping track of these through an accumulator matrix. In essence, for each line defined in polar coordinates as

$$d = x\cos(\theta) + y\sin(\theta)\,, \tag{6-6}$$

each pair of neighboring pixels which are both on an edge increments an accumulator for the appropriate line as defined by d and θ. Large values in the accumulator indicate lines. Generalizations of this basic idea to gray scale images and more general shapes are possible, and have been carried out by a number of researchers.[16]

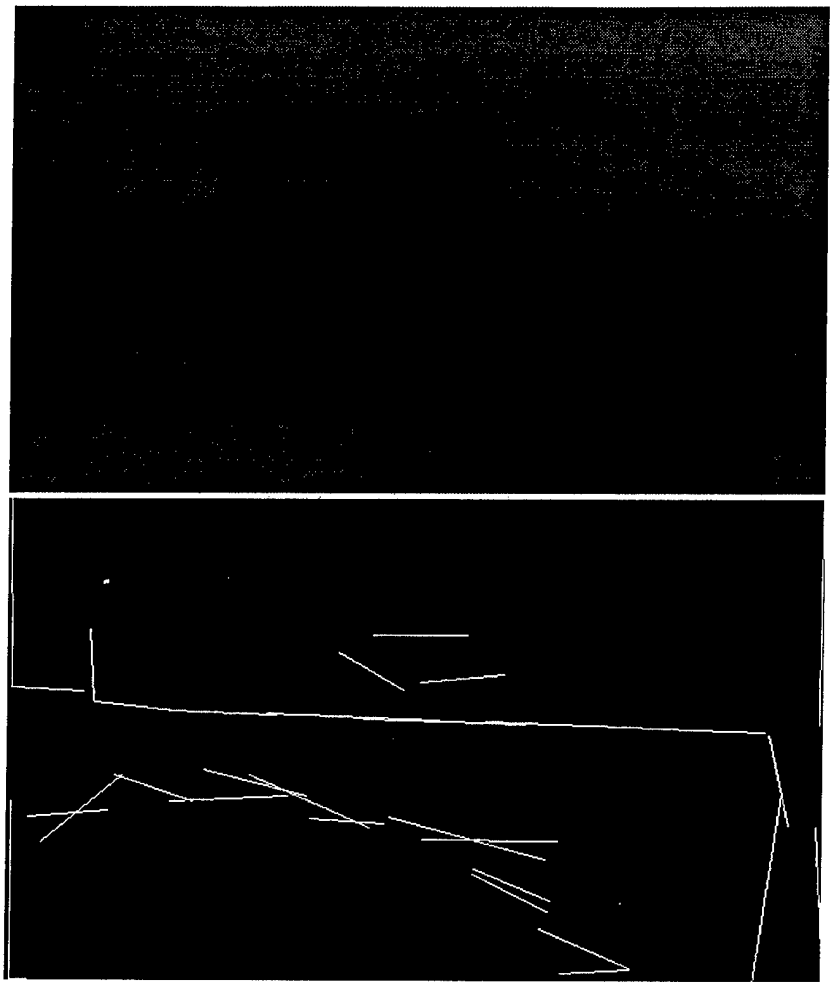

Figure 6-6. Original (Thermal) Image of Area M Taken at 1832 and Hough Transform

As can be seen in the examples in Figures 6-6 and 6-7, the Hough transform works quite well on the visible images, where the noise level is fairly low, however it does not work as well on most of the thermal images, as a result of the higher noise level. There are some noise reduction techniques which could be applied to these images, and this could be an area of further investigation

6.4 TEXTURE FEATURES

For some kinds of damage the above algorithms provide some tools which can be used for detection, however these are not necessarily appropriate for other kinds of damage. For example, bomb craters do not necessarily have linear sides, gravel is not necessarily a different temperature than the runway, etc. These problems will require other kinds of algorithms.

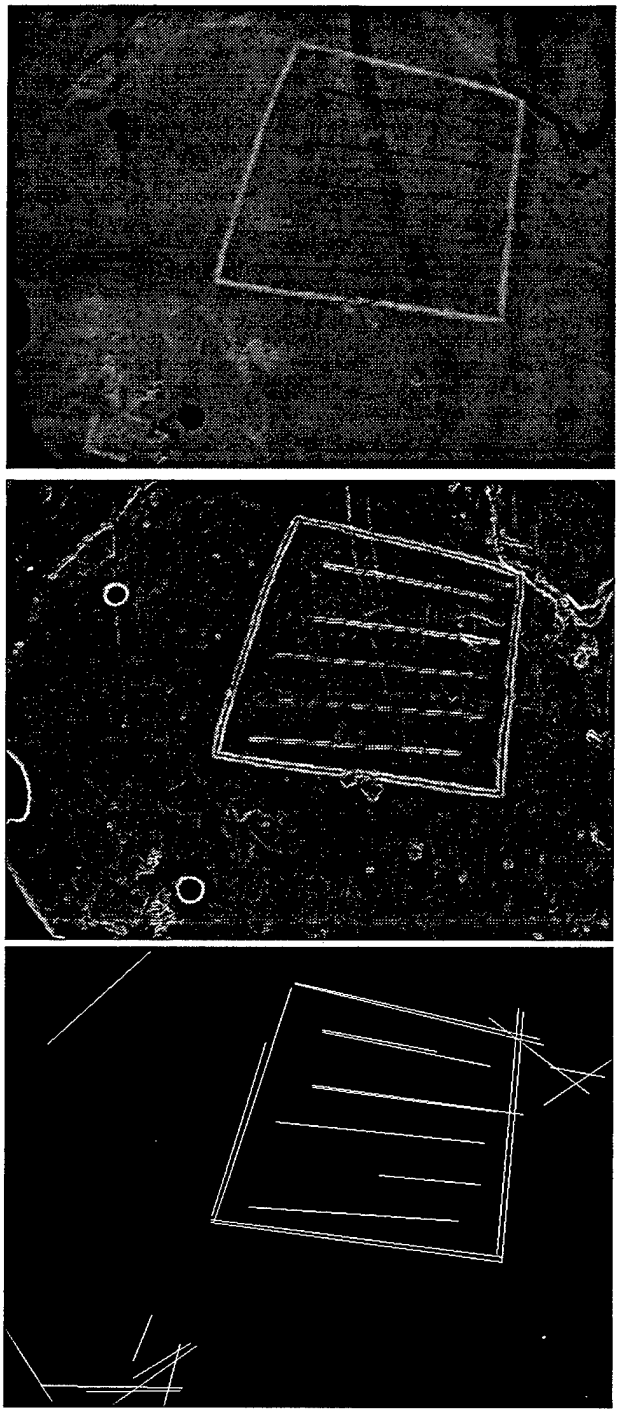

Figure 6-7. Original (Visual) Image of Area E Taken at 1738, Sobel Edge Detection for the Image, and Hough Transform

One such method, which may be useful in detecting gravel or patches on the runway, is the use of texture features. A lot of work has been done in this area[17,18] for a number of applications, and there is reason to believe it could be useful for some of these problems as well. For example, gravel should have a different texture than a clean runway, and it should be possible to detect it. However, lots of other things will have different textures as well, for example leaves, dirt, patches to the runway, paint spills, etc., and it is not clear what texture features are appropriate to distinguish between these different conditions.

To some degree the use of thermal imaging can reduce the problems with some of the above conditions, however as has been seen thermal imagery is quite noisy and may not detect many of the objects of interest. A thorough study of these issues would be of interest, and could possibly indicate both the utility and the limitations of the different imagery modalities.

There are many different texture measures which can be used on this imagery to characterize different types of damage to the runway. The large number of possible features requires some time to process and analyze, and so would require more time than was available for this study. Once the necessary features have been identified, they could be used to classify the regions of the runway in near real time.

An example of one of the texture features investigated is shown in Figure 6-8. This is a Laws texture feature,[19] which is constructed by convolving the image with a particular mask. It is clear from the figure that small gravel has a different texture, under this measure, than larger rocks or smooth runways. Thus, by using the appropriate texture features, it would be possible to distinguish between different kinds of clutter on the runway. Similar algorithms could be used to distinguish other types of damage such as extensive cracking of the runway or other types of clutter on the runway.

With a limited image set and time for analysis, we could only give some indications of the kind of algorithms that can be applied to these images. The morphology algorithms can detect objects which are larger or smaller than a given size. Edge extraction algorithms and Hough transforms can be used to find linear structures. The Hough transform can be generalized to other shapes than lines. Different texture features can be extracted to distinguish between different kinds of objects or damage. The MAP estimator can be used not only on the raw gray scale images, but also on the features and even on classification maps to smooth the results and eliminate false alarms due to noise.

Clearly no single algorithm will work to extract all the information of interest from the images. A series of algorithms would need to be developed, each one designed to find a particular structure. These algorithms would then work together to give an overal classification of the damage to the runway.

In an operational system, one would most likely use video rather than still imagery. With video mosaicking techniques, the frames from the video can be overlaid to produce a single large image of the entire runway. The integration of multiple frames allows some denoising through the reduntant information in the frames. It also allows for improved classification by reducing

false alarms. The mosaic would give a picture of the entire runway with the locations of any trouble areas in the context of the entire scene. This would allow decisions to be based on where the damage occurs on the runway, rather than how much damage there is overall.

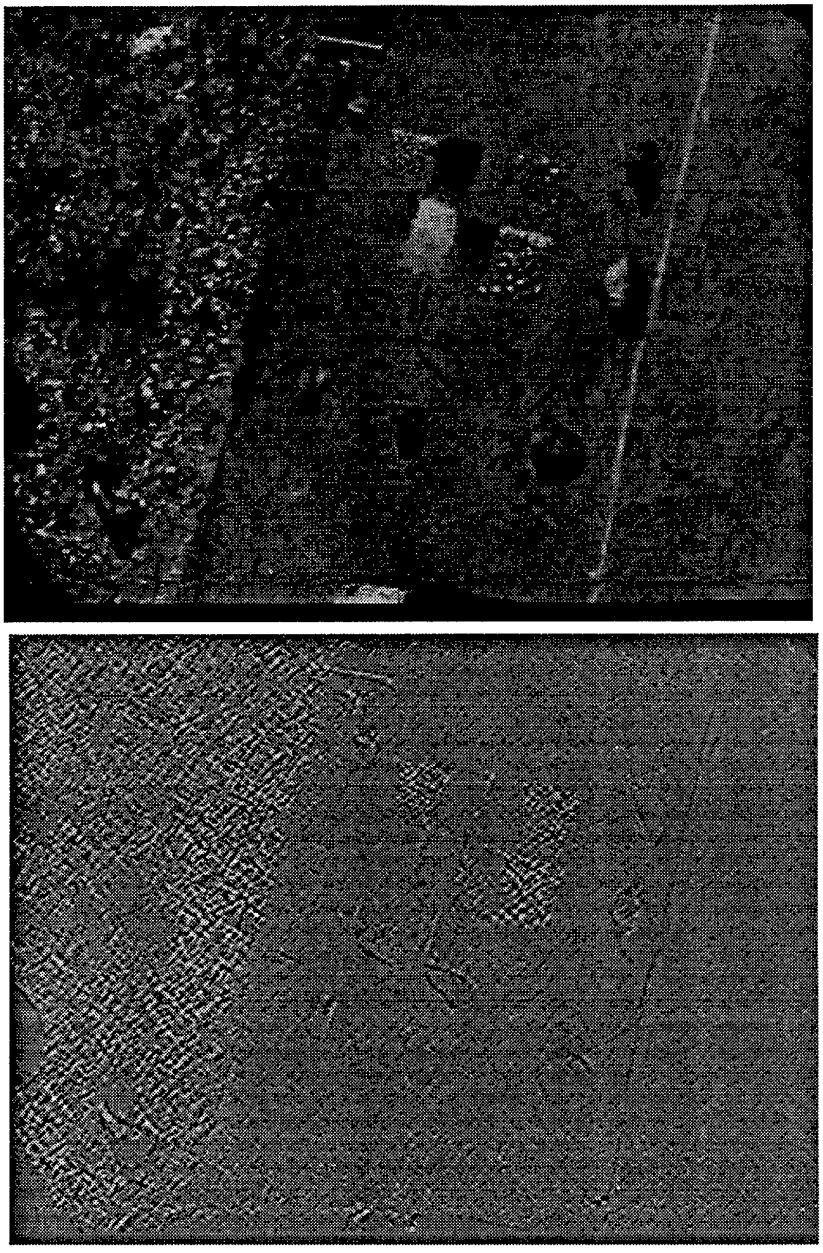

Figure 6-8. Original (Thermal) Image of Area H Taken at 550 and Laws Texture Feature

The mosaic could also be of value in its own right. Given a mosaic showing the runway at a sufficiently high resolution, a human operator could classify the damage, given the training necessary to interpret the non-visible spectrum imagery. Multiple mosaics in different spectra could be registered to allow a multi-spectral view of the runway. This could greatly enhance the detection and identification of damage, by utilizing the strengths of the different imagery.

CHAPTER 7

SUMMARY

The various passive and active imaging systems have been analyzed for application to remote sensing of airfields. The purpose is to determine whether a plane can be safely landed. The criteria of interest are: type of material (including differences in material, such as patches), delamination, cracks, holes, spalls, debris, surface roughness (large scale, such as trenches) and subsurface voids. It is apparent that a single system will not yield all the critical information. A combination of systems is necessary to detect all of these defects. Table 7-1 contains a summary of the systems that have been reviewed and what type of fault each can detect, assuming each has been optimized as outlined in Section 2. Polarimetry has not been included in the list because it is not a stand-alone technique. Rather, it is used to enhance discrimination capabilities when coupled with an imaging system.

Table 7-1. Summary of System Type and Capability

	Material Type	Delamination	Cracks	Holes	Spalls	Debris	Surface Roughness	Subsurface Voids
Multispectral	YES	NO	NO*	NO*	NO*	YES	NO*	NO
Hyperspectral	YES	NO	NO*	NO*	NO*	NO*	NO*	NO
Thermal	YES**	YES	YES	YES	YES	YES	NO†	YES
Stereoscopic	NO	NO	YES	YES	YES	YES	YES	NO
Scanning Lidar	NO	NO	YES	YES	YES	YES	YES	NO
Beam Fanning	NO	NO	YES	YES	YES	YES	YES	NO
Visible	NO	NO	YES	YES	YES	YES	NO†	NO

* May be detected in individual frames, but not by design of the technique.

** Can detect differences in materials or hardness of dirt, but cannot identify materials by spectral signature as in the multispectral and hyperspectral systems.

† Can marginally detect, as seen in field test data, but depth information is not obtained.

The multispectral, hyperspectral, and thermal systems can distinguish between material types based on the spectral signatures of the materials. If there is dirt or weeds growing in a

crack on a runway, for example, these would be distinguishable from the "good pavement" background. These systems can also detect oil, water, patches or other anomalies based on different materials present in the image. The runway construction can be determined with the two spectral systems; i.e., dirt, asphalt, concrete, type of aggregate, etc.

The thermal imager has the further capability of detecting surface faults such as cracks and holes, and subsurface defects. The thermal imaging system does not provide depth information. Thus, a hot spot may be caused by sand or dirt on the surface, or it may be caused by a subsurface void. The only way to tell is to couple the thermal information with another system. One possibility is to combine a thermal system with a standard video camera (or other visible imaging system). If the detected hot spot correlates with something in the visible image, then the defect is at the surface. If there is not a defect in the visible image to correspond to the hot spot in the thermal image, then the defect is subsurface. Another possibility is to incorporate two thermal cameras in a stereoscopic system. Depth information is available from the stereoscopic setup and any hot spots in the thermal image can be pinpointed at the surface or below the surface. A drawback to the thermal imaging system is that, as shown by the data from the field test, the surface defects are best detected in the early morning during periods of heating, while the subsurface faults are more easily detected in the evening during periods of cooling. A second drawback is that thermal imaging is not possible in rain, fog, or when there is standing water on the runway. Successful operation is dependent on local weather conditions.

A compelling reason for employing active imaging systems is for increased signal-to-noise and target detectability when imaging through dense media. These systems are heavily employed for underwater imaging where the attenuation is appreciable. For imaging through air, unless there is heavy fog or smoke, the difficulty and expense in the implementation of an active system are not justifiable. The reason the two active systems have been evaluated in this study is that they yield depth information, which most of the passive systems do not. Since the passive stereoscopic system also imparts depth information, we do not recommend further investigations into active imaging for this application.

CHAPTER 8

RECOMMENDATIONS

For application to remote sensing of airfields, the thermal imaging system yields the most information. We recommend further study of this system. The thermal camera used in the field test was built in the late eighties. Newer cameras have better spatial and temperature resolution. We recommend investigations into possible enhancement by incorporation of polarimetry into the thermal imaging system. It would be further illuminating to take data of a single area over an entire 24-hour period to fill in the missing data for the graphs in Figures 5-39 through 5-46. We may then be able to find an optimal time/temperature for detecting both surface and subsurface defects.

In a deployed system, we recommend coupling the thermal system to a visible system to (1) distinguish between surface and subsurface defects, and (2) have some means of evaluating the airstrip when inclement weather prohibits use of the thermal imager. This coupled system will not give depth information, thus surface roughness information will not be available. If this data is absolutely necessary, we recommend some combination of visible and thermal imaging with the stereoscopic technique: stereoscopic thermal imaging with and additional visible camera; or stereoscopic visible imaging with an additional thermal camera. It may be possible to design a stereoscopic imaging system in which one of the cameras is a visible CCD array and the other is a thermal array. The cameras would have to be specially made with the same number and size of pixels. Since the technology for visible CCD is currently more advanced than for IR detectors, the resolution will be limited by present IR technology.

It is also advisable to perform a rigorous theoretical analysis to determine whether the runway material (asphalt, concrete, etc.) can be determined from the thermal images based on knowledge of the material properties (emissivity, thermal conductivity, and heat capacity) and the ambient temperature.

REFERENCES

1. Witherspoon, N. H. et al., "Coastal Battlefield Reconnaissance and Analysis (COBRA), Program for Minefield Detection," SPIE Detection Technologies for Mines and Mine-like Targets proceedings, 2496, 500, 1995.

2. Reed, L. S. and Yu, X., "Adaptive Multiple-Band CFAR Detection of an Optical Pattern with Unknown Spectral Distribution," IEEE Tran. Acoustics, Speech and Signal Processing, 38, 10, 1990.

3. Trent, A.; Bowman, A.; Lucey, P. I.; and Winter, E. M., "Phenomenology Considerations for Hyperspectral Mine Detection," unpublished, 1994.

4. Satterwhite, M. B. and Henley, J. P., *Hyperspectral Signatures of Vegetation, Minerals, Soils, Rocks, and Cultural Features: Laboratory and Field Measurements*, Report ETL-0573, U.S. Army Corps of Engineers, Engineer Topographic Laboratories, 1990.

5. Godfrey, K. A., "New Tools Help Find Flaws," *Civil Engineering*, 39, Sep 1984.

6. Weil, G. J. and Haefner, L. E., "Toward an Integrated Non-Destructive Pavement Testing Management Information System Using Infrared Thermography," preprint, Transportation Research Board 68th Annual Meeting, 1989.

7. Simard, J. R., "Three-Dimensional Imaging at 10.6 μm to Detect Surface-Laid Mines," SPIE Proceedings for Detection Technologies for Mines and Minelike Targets, 2496, 168, 1995.

8. Lide, D. R., Ed., *CRC Handbook of Chemistry and Physics,* 77th Edition, CRC Press, Boca Raton, FL, 1996.

9. Dougherty, E. R., *An Introduction to Morphological Image Processing*, Volume TT9, SPIE Optical Engineering Press, Bellingham, WA, 1992.

10. Serra, J., *Image Analysis and Mathematical Morphology*, Volume 1, Academic Press Limited, London, 1982.

11. Dougherty, E. R., "Euclidean Gray-Scale Granulometries: Representation and Umbra Inducement," *J. Math. Imaging Vision*, Vol. 1, pp. 7-21, 1992.

REFERENCES (Continued)

12. Wallet, B. C.; Solka, J. L.; and Priebe, C. E., "A Method for Detecting Microcalcifications in Digital Mammography," To Appear in the Proceedings of the 14th Symposium for Computer Applications in Radiology.

13. Vogt, R. C., "A Spatially Variant, Locally Adaptive, Background Normalization Operator," in *Mathematical Morphology and Its Application to Image Processing*, Jean Serra and Pierre Soille, Eds., Kluwer Academic Press, The Netherlands, 1994.

14. Priebe, C. E.; Holcomb, H. H.; and Marchette, D. J., "Contextual Investigation of Ketamine Effects in PET Scan Brain Imaging," Joint Statistical Meetings, 1996.

15. Haralick, R. M. and Shapiro L. G., *Computer and Robot Vision*, Vol. 1, Addison-Wesley, Reading, Ma, 1992.

16. Leavers, V. F., "Which Hough Transform?" *CVGIP: Image Understanding*, Vol. 58, pp. 250-264, 1993.

17. Solka, J. L.; Marchette, D. J.; Rogers, G. W.; Durling, E. C.; Green, J. E.; and Talsma, D., "Region of Interest Identification in Unmanned Aerial Vehicle Imagery," AIPR, 1996.

18. Reed, T. R. and Hans Du Buf, J. M., "A Review of Recent Texture Segmentation and Feature Extraction Techniques," *CVGIP: Image Understanding*, Vol. 57, pp. 359-372, 1993.

19. Laws, K. I., *Textured Image Segmentation*, Report 940, Processing Institute, UCLA, 1980.

BIBLIOGRAPHY

Azevedo, S. G.; Gavel, D. T.; Mast, J. E.; and Warhus, J. P., "Statement of Capabilities: Micropower Impulse Radar (MIR) Technology Applied to Mine Detection and Imaging," LLNL internal document UCRL-ID-5366, 1995.

Chenault, D. B., "Ice Detection Using Infrared Imaging Polarimetery," Proceedings of the Workshop on Infrared and Millimeter Wave Polarimetry, Dec 1995.

Chipman, R. A. and Chenault, D. B., *Infrared Polarization Signatures*, Air Force Technical Report, AFATL TR 90-14, Jun 1990.

Flynn, D. S., "Modeling Polarization Effects in Irma's Passive Channel," Proceedings of the Workshop on Infrared and Millimeter Wave Polarimetry, Dec 1995.

Green, R. O., Ed., "Summaries of the Sixth Annual JPL Airborne Earth Science Workshop," NASA and JPL, 1996.

Hess, M. R. et al. "Measurement and Analysis of Aircraft Infrared Signature Polarization," IRIS Proceedings, 1994.

Lavreau, J; Rudant, J. P.; and Trefois, P., "Rock and Soil Discrimination in Natural Tropical Conditions Using a Spot Calibrated Radiometer," ESA Proceedings of Spectral Signatures of Objects in Remote Sensing, SP-287, 383, 1988.

Peterson, J. C. et al., *Sensor Technology Assessment for Ordinance and Explosive Waste Detection and Location,* DTIC Report 19960405079, 1995.

Rish, J. W.; Adcock, A. D.; Tuan, C. Y.; Baker, S. L.; and Welker, H. W., "Electro-optical Approach to Pavement Deflection Management," SPIE Proceedings of Nondestructive Evaluation of Aging Aircraft, Airports, Aerospace Hardware and Materials, 2455, 363, 1995.

Rogne, T. J.; Smith, F. G.; and Rice, J. E., "Passive Target Detection Using Polarized Components of Infrared Signatures," SPIE Proceedings, Vol. 1317, 1990.

Salisbury, J. W. and D'Aria, D. M., "Emissivity of Terrestrial Materials in the 3-5 μm Atmospheric Window," *Remote Sens. Environ.*, 47, 345, 1994.

Swanson, H. N. and Woodham, D. B., *Use of Road Oil by Maintenance*, Department of Transportation (DOT) Technical Report CDOH-DTD-R-89-5, 1989.

BIBLIOGRAPHY (Continued)

Swayze, G. A.; Clark, R. N.; Pearson, R. M.; and Livo, K. E., "Mapping Acid-Generating Minerals at the California Gulch Superfund Site in Leadville, Colorado Usning Imaging Spectroscopy," JPL Press Release, 1996.

Timian, D. A. et al., "Asphaltic Concrete Performance Under Heavy Fighter Aircraft Loading," Report prepared for Air Force Engineering and Services Center, TAFB, under contract F08635-88-C-0067, 1991.

Tooley, R. D., "Man-Made Target Detection Using Infrared Polarization," SPIE Proceedings, Vol. 1166, 1989.

Watson, J. and Flynn, D. S., "The Irma Multisensor Predictive Signature Model," Proceedings of the Sixth Annual Ground Target Modeling and Validation Conference, Aug 1995.

Zissis, G. J., Ed., *The Infrared & Electro-Optical Systems Handbook*, Vol. 1, ERIM, Ann Arbor, and SPIE Optical Engineering Press, Bellingham, WA, 1993.

DISTRIBUTION

	Copies
DOD ACTIVITIES (CONUS)	
ATTN DR JEFF RISH COASTAL SYSTEMS STATION CODE R23 6798 W HWY 98 PANAMA CITY FL 32407	1
DEFENSE TECHNICAL INFORMATION CENTER 8725 JOHN J KINGMAN RD SUITE 0944 FORT BELVOIR VA 22060-6218	2
ATTN CODE A76 (TECHNICAL LIBRARY) COMMANDING OFFICER CSSDD NSWC 6703 HIGHWAY 98 PANAMA CITY FL 32407-7001	1
NON-DOD ACTIVITIES (CONUS)	
ATTN GIFT AND EXCHANGE DIV LIBRARY OF CONGRESS WASHINGTON DC 20540	4
THE CNA CORPORATION P O BOX 16268 ALEXANDRIA VA 22302-0268	1
ATTN JONATHAN PORTER WRIGHT LABORATORY WL FIVCO OL (STOP 37) 139 BARNES DRIVE SUITE 2 TYNDALL AFB FL 32403	1
ATTN BRAD BLUME NICHOLS RESEARCH CORP P O BOX 9474 PANAMA CITY FL 32417	1
ATTN JOAN PINAMONT COLORADO DEPT OF TRANSPORTATION TECHNICAL TRANSFER LIBRARY DENVER CO 80222	1
ATTN HERBERT SWANSON 318 KILLDEER LANE OCEAN SIDE CA 92057	1
INTERNAL	
B10 (IRWIN)	1
B10 (MARCHETTE)	1
B20 (SWANSON)	2
B60 (LIBRARY)	3